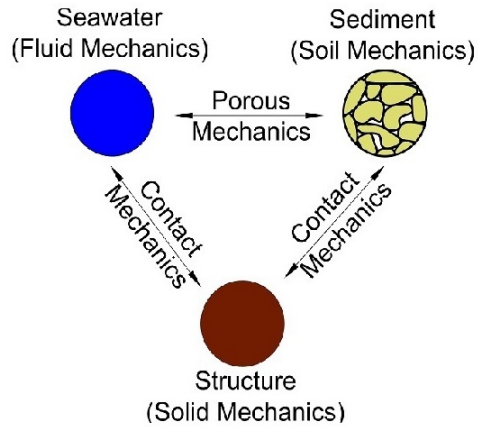
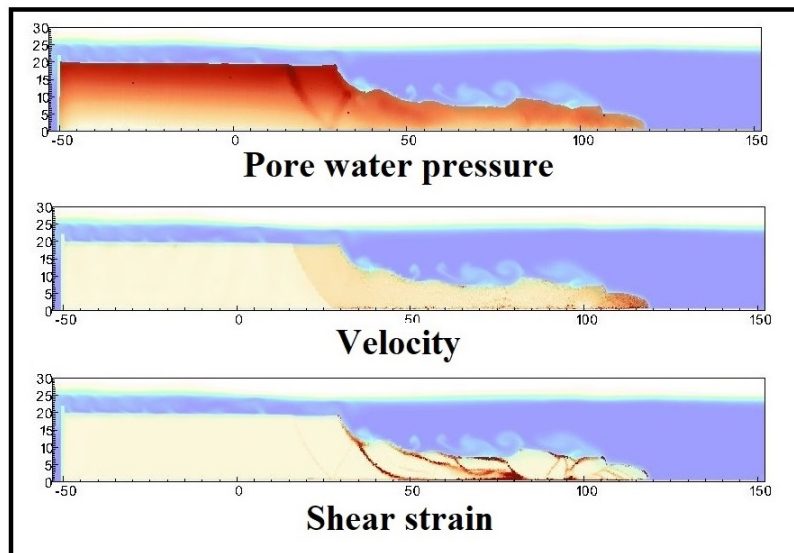


## Graphical Abstract

**MPMICE: A Lagrangian-Eulerian framework for non-isothermal coupling of deformable porous media and fluid flow**



**MPMICE capture complex  
soil-fluid-structure interaction**



**Application to earthquake-induced submarine landslide**

## Highlights

### **MPMICE: A Lagrangian-Eulerian framework for non-isothermal coupling of deformable porous media and fluid flow**

- MPMICE is introduced for multiphase flow in porous media.
- Material Point method allows to model large deformation of non-isothermal porous media.
- ICE (compressible multi-material CFD formulation) allows to stabilize pore water pressure and turbulent flow.
- MPMICE is validated and apply to simulate the earthquake-induced submarine landslide.

# MPMICE: A Lagrangian-Eulerian framework for non-isothermal coupling of deformable porous media and fluid flow

---

## Abstract

Since offshore structures are expanding significantly, it is critical to estimate potential submarine landslides so that offshore structures can withstand landslides. The complex interaction between saturated sediment, seawater, and offshore structures makes it challenging to simulate submarine landslides. In this paper, a soil-fluid-structure interaction model is presented that combines soil mechanics (saturated sediments), fluid mechanics (seawater), and solid mechanics (structures). The formulation involves coupling the Material Point Method, which models large deformation of porous media, with the Implicit Continuous-fluid Eulerian, which models complex fluid flow. We validate the model and simulate the whole process of earthquake-induced submarine landslides.

*Keywords:*

Material Point Method, MPMICE, submarine landslide.

---

## Contents

<b>Nomenclature</b>	<b>4</b>
<b>Introduction</b>	<b>6</b>
<b>Theory and formulation</b>	<b>8</b>
Assumptions . . . . .	8
Governing equations . . . . .	9
Equation of state for fluid phases . . . . .	11
Constitutive soil model . . . . .	12
Momentum and Energy exchange model . . . . .	13
Solving momentum exchange with an implicit solve . . . . .	13
Turbulent model . . . . .	14
Contact law for soil-structure interaction . . . . .	14
<b>Numerical implementation</b>	<b>15</b>
Interpolation from Solid Particle to Grid . . . . .	15
Compute equation of state for fluid phase . . . . .	16
Compute faced-centered velocity . . . . .	16
Compute advanced fluid pressure (implicit scheme) . . . . .	17
Compute viscous shear stress term of the fluid phase . . . . .	18
Compute nodal internal temperature of the solid phase . . . . .	18
Compute and integrate acceleration of the solid phase . . . . .	18
Compute Lagrangian value (mass, momentum and energy) . . . . .	18
Compute Lagrangian specific volume of the fluid phase . . . . .	19
Compute advection term and advance in time . . . . .	20
Interpolate from cell to node of the solid phase . . . . .	21
Update the particle variables . . . . .	21
<b>Numerical examples</b>	<b>21</b>
Fluid Flow through isothermal porous media . . . . .	22
Isothermal consolidation . . . . .	23
Thermal induced cavity flow . . . . .	24
Underwater debris flow . . . . .	25
Earthquake-induced submarine landslides . . . . .	29
<b>Conclusions</b>	<b>33</b>

<b>Acknowledgements</b>	<b>34</b>
<b>Appendix</b>	<b>34</b>
Evolution of porosity . . . . .	35
Evolution of specific volume . . . . .	35
Momentum conservation . . . . .	36
Energy conservation . . . . .	37
Advanced Fluid Pressure . . . . .	38
Momentum exchange with an implicit solve . . . . .	39

## Nomenclature

### General variables

<u>Variable</u>	<u>Dimensions</u>	<u>Description</u>
$V$	$[L^3]$	Representative volume
$n$		Porosity
$\sigma$	$[M/L^2]$	Total stress tensor
$\Delta t$	$[t]$	Time increment
$\mathbf{b}$	$[L/t]$	Gravity acceleration
$c_v$	$[L^2/t^2]$	Constant volume specific heat
$f_d$	$[ML//t^2]$	Drag forces in momentum exchange term
$f^{int}$	$[ML//t^2]$	Internal forces
$f^{ext}$	$[ML//t^2]$	External forces
$q_{fs}$	$[ML//t^2]$	Heat exchange term
$S$		Shape function
$\nabla S$		Gradient of shape function

### Solid phase

<u>Variable</u>	<u>Dimensions</u>	<u>Description</u>
$m_s$	$[M]$	Solid mass
$\rho_s$	$[M/L^3]$	Solid density
$\phi_s$	$-]$	Solid volume fraction
$\bar{\rho}_s$	$[M/L^3]$	Average Solid density
$\mathbf{x}_s$	$[L]$	Solid Position vector
$\mathbf{U}_s$	$[L/t]$	Solid Velocity vector
$\mathbf{U}'_s$	$[L/t]$	Solid Velocity gradient vector
$\mathbf{a}_s$	$[L/t^2]$	Solid Acceleration vector
$\sigma'$	$[M/L^2]$	Effective Stress tensor
$e_s$	$[L^2/t^2]$	Solid Internal energy
$T_s$	$[T]$	Solid Temperature
$\mathbf{F}_s$		Solid Deformation gradient
$V_s$	$[L^3]$	Volume

<b>Fluid phase</b>		
<u>Variable</u>	<u>Dimensions</u>	<u>Description</u>
$m_f$	[M]	Fluid mass
$\rho_f$	[M/L <sup>3</sup> ]	Fluid density
$\phi_f$	[—]	Fluid volume fraction
$\bar{\rho}_f$	[M/L <sup>3</sup> ]	Average Fluid density
$\mathbf{U}_f$	[L/t]	Fluid Velocity vector
$\boldsymbol{\sigma}_f$	[M/L <sup>2</sup> ]	Fluid stress tensor
$\Delta p_f$	[M/L <sup>2</sup> ]	Fluid isotropic pressure
$\boldsymbol{\tau}_f$	[M/L <sup>2</sup> ]	Fluid shear stress tensor
$p_f$	[M/L <sup>2</sup> ]	Isotropic pressure
$e_f$	[L <sup>2</sup> /t <sup>2</sup> ]	Fluid Internal energy ( $c_v T_f$ ) of the material per unit mass
$T_f$	[T]	Fluid Temperature
$v_f$	[L <sup>3</sup> /M]	Fluid Specific volume $\frac{1}{\rho_f}$
$\alpha_f$	[1/T]	Thermal expansion
$\mu$	[M/L <sup>2</sup> T]	Fluid viscosity
<b>Superscript</b>		
<u>Variable</u>	<u>Dimensions</u>	<u>Description</u>
$n$		Current time step
$L$		Lagrangian values
$n + 1$		Next time step
<b>Subscript</b>		
$c$		Cell-centered quantity
$p$		Particle quantity
$i$		Node quantity
$FC$		Face-centered quantity
$L, R$		Left and Right cell faces

Table 1: Nomenclature

## Introduction

Submarine landslides can pose significant threats to the offshore infrastructures and the coastal communities. Submarine landslides have three stages: triggering, failure, and post-failure. Erosion or earthquakes can trigger slope failures in the first stage. Following the failure, sediments move quickly after the post-failure stage. As a submarine landslide is triggered, sediment behaves like solid (soil) materials and changes to fluid-like behavior after failure. This phase transition makes it challenge to simulate the submarine landslides.

Due to this phase transition, submarine landslide can be modeled by either the Computational Fluid Dynamics (CFD) or the particle-based methods. For simulating submarine slides, CFD methods solve governing equations in a full-Eulerian framework for single-phase flows [1, 2] and for multi-phase flows [3, 4] with interface capturing techniques. While CFD can handle complex flows (such as turbulent flows), it cannot account for the triggering mechanism of submarine landslides because it is not straightforward to consider 'soil constitutive laws' of sediment materials in the Eulerian framework. In contrast, particle-based methods can overcome this problem by using the Lagrangian framework. These methods have been extensively used to simulate landslides, like Material Point Method (MPM) [5], Smooth Particle Hydro Dynamics [6], Particle Finite Element Method [7], or Coupled Eulerian Lagrangian Method [8]. For simplicity, these simulations adopt total stress analysis which neglects the pore pressure development which is the key factor triggering slope failures.

Recent developments in particle-based methods model the coupling of fluid flow in porous media by sets of Lagrangian particles. For the MPM family, it is the double-point MPM ([9, 10, 11]) where fluid particles and solid particles are overlapped in a single computational grid. Even if fluid flows are considered, particle-based methods have numerical instability in modeling the fluid flow, which requires additional numerical treatments such as the B-bar method [9], null-space filter [12], or least square approximation [13, 14]. Indeed, CFD is a more optimal option for complex fluid flows especially dealing with large distortions of continuum fluid media. Therefore, it could be ideal to combine the CFD with particle-based methods. More than 50 particle-based methods have been developed to solve large deformations

of solids over the last two decades [15], but the MPM appears to be the best candidate for coupling with the CFD. Because MPM incorporates a stationary mesh during computation, just like CFD. As such, both MPM and CFD can be coupled naturally in a unified computational mesh.

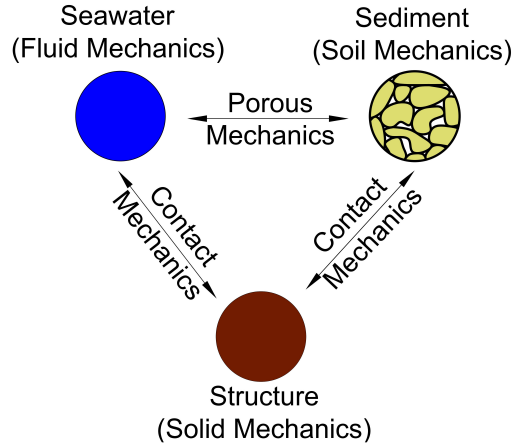


Figure 1: Interaction between soil-fluid-structure

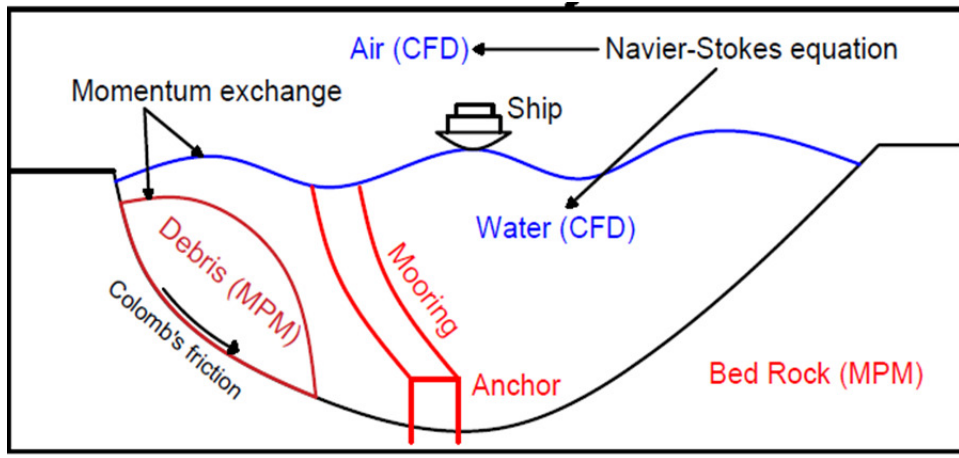


Figure 2: Coupling of soil-water-structure interaction using MPMICE

A numerical method for simulating soil-fluid-structure interaction (Figure 1) involving large deformations, is presented in this work in order to

simulate the interaction between sediment (soil), seawater (fluid) and off-shore structures (structure) namely MPMICE (Figure 2). In the MPMICE, the Material Point Method (MPM) is coupled with the Implicit Continuous Eulerian (ICE). The MPM method is a particle method that allows the porous soil to undergo arbitrary distortions. The ICE method, on the other hand, is a compressible, conservative finite volume technique with all state variables located at the cell center (temperature, velocity, mass, pressure). An initial technical report [16] at Los Alamos National Laboratory provided the theoretical and algorithmic foundation for the MPMICE, followed by the MPMICE development and implementation in the high-performance Uintah computational framework for simulating fluid-structure interactions [17]. This paper primarily contributes further to the development of the MPMICE for analyzing the **soil**-fluid-structure interaction, since sediment should be considered as a porous media (soil) and not as a solid to capture the evolution of the pore water pressure. Baumgarten et al. [18] made the first attempt at coupling the Finite Volume Method with the MPM for the simulation of soil-fluid interaction. Our contribution differs from the mentioned work in that we use the implicit time integration for the fluid phases instead of the explicit time integration.

## Theory and formulation

This section lay out the theoretical framework for the MPMICE model. We use the common notation of the continuum mechanics with vector and tensor denoted simply by using bold font and scalar denoted by using normal font. The notation are shown in Table 1.

### *Assumptions*

The following assumptions are made for the MPMICE model.

1. Solid phases (MPM) are described in a Lagrangian formulation while fluid phases (ICE) are described in an Eulerian formulation in the framework of continuum mechanics and mixture theory.
2. Solid grains are incompressible while the fluid phase is compressible.
3. There is no mass exchange between solid and fluid phases.
4. Terzaghi's effective stress is valid.

### Governing equations

A representative element volume  $\Omega$  is decomposed by two domains: solid domains  $\Omega_s$  and fluid domains  $\Omega_f$ . Then, all domains are homogenized into two overlapping continua. Considering the volume fraction of solid  $\phi_s = \Omega_s/\Omega$  and fluid  $\phi_f = \Omega_f/\Omega$  with the true (or Eulerian) porosity  $n = \sum \phi_f$  of the representative element volume, the average density of solid and fluid phases are defined as:

$$\bar{\rho}_s = \phi_s \rho_s, \quad \bar{\rho}_f = \phi_f \rho_f \quad (1)$$

The mass of solid and fluid phase are:

$$m_s = \int_{\Omega} \rho_s dV = \bar{\rho}_s V, \quad m_f = \int_{\Omega} \rho_f dV = \bar{\rho}_f V \quad (2)$$

Reviewing the Terzaghi's effective stress concept for the saturated porous media, the total stress  $\boldsymbol{\sigma}$  is calculated by:

$$\boldsymbol{\sigma} = \boldsymbol{\sigma}' - p_f \mathbf{I} \quad (3)$$

The balance equations are derived based on the mixture theory. The average thermodynamic state of the fluid phases are given by the vector  $[m_f, \mathbf{U}_f, e_f, T_f, v_f]$  which are mass, velocity, internal energy, temperature, specific volume. The average state of the solid phases are given by the vector  $[m_s, \mathbf{U}_s, e_s, T_s, \boldsymbol{\sigma}']$  which are mass, velocity, internal energy, temperature, effective stress. Here, we summarize the final form of the equations while the derivation is presented in detail in the Appendix.

### Mass Conservation

The mass balance equations for both fluid and solid phases are:

$$\frac{1}{V} \frac{D_f m_f}{Dt} = 0, \quad \frac{1}{V} \frac{D_s m_s}{Dt} = 0 \quad (4)$$

### Momentum Conservation

The momentum balance equation for the fluid phase is:

$$\frac{1}{V} \frac{D_f (m_f \mathbf{U}_f)}{Dt} = -n \nabla P_{eq} + \nabla \cdot \boldsymbol{\tau}_f + \bar{\rho}_f \mathbf{b} + \mathbf{f}_d \quad (5)$$

The momentum balance equation for the solid phase is:

$$\frac{1}{V} \frac{D_s(m_s \mathbf{U}_s)}{Dt} = \nabla \cdot (\boldsymbol{\sigma}') - (1-n) \nabla p_f + \bar{\rho}_s \mathbf{b} - \mathbf{f}_d \quad (6)$$

### Energy Conservation

The internal energy balance equation for the fluid phase is:

$$\frac{1}{V} \frac{D_f(m_f e_f)}{Dt} = -\bar{\rho}_f P_{eq} \frac{D_f v_f}{Dt} + \boldsymbol{\tau}_f : \nabla \mathbf{U}_f + \nabla \cdot \mathbf{q}_f + q_{sf} \quad (7)$$

The internal energy balance equation for the solid phase is:

$$\frac{1}{V} \frac{D_s(m_s e_s)}{Dt} = \boldsymbol{\sigma}' : \nabla \mathbf{U}_s + \nabla \cdot \mathbf{q}_s - q_{sf} \quad (8)$$

To close the systems of the equations, it requires the additional models:

- (1) Exchange momentum model (computing drag force  $\mathbf{f}_d$ ).
- (2) Energy exchange model (computing temperature exchange term  $q_{sf}$ ).
- (3) Optional turbulent model to compute the viscous shear stress  $\boldsymbol{\tau}_f$ .
- (4) A constitutive equation to describe the stress - strain behaviour of solid phase (computing effective stress  $\boldsymbol{\sigma}'$ ).
- (5) An equation of state to establish relations between thermodynamics variables of each fluid materials  $[P_{eq}, \bar{\rho}_f, v_f, T_f, e_f]$ .

Here,  $P_{eq}$  is "equilibrium" pressure which is defined as pressure enables mass of fluid material to fill in an entire porosity volume with no ongoing compression or expansion with given true density  $\rho_f$  and temperature  $T_f$ . Four thermodynamic relations for the equation of states are:

$$\begin{aligned} e_f &= e_f(T_f, v_f) \\ v_f &= v_f(T_f, P_{eq}) \\ \phi_f &= v_f \bar{\rho}_f \\ 0 &= n - \sum_{f=1}^{N_f} v_f \bar{\rho}_f \end{aligned} \quad (9)$$

Solving the equation of state (see Appendix's section 'Evolution of specific volume') leading to the rate of the equilibrium pressure of fluid mixture as:

$$\sum_{f=1}^{N_f} \phi_f \kappa_f \frac{D_f P_{eq}}{Dt} = -\nabla \cdot \mathbf{U} + \sum_{f=1}^{N_f} \phi_f \alpha_f \frac{D_f T_f}{Dt} \quad (10)$$

where  $\mathbf{U} = \nabla \cdot (\sum_{s=1}^{N_s} \phi_s \mathbf{U}_s + \sum_{f=1}^{N_f} \phi_f \mathbf{U}_f)$ . And the rate of the specific volumne of fluid materias are:

$$\bar{\rho}_f \frac{D_f v_f}{Dt} = f_f^\phi \nabla \cdot \mathbf{U} + (\phi_f \alpha_f \frac{D_f T_f}{Dt} - f_f^\phi \sum_{n=1}^N \phi_n \alpha_n \frac{D_n T_n}{Dt}) \quad (11)$$

where  $f_f^\phi = (\phi_f \kappa_f) / (\sum_{n=1}^N \phi_n \kappa_n)$  with  $\kappa_f$  being f-material bulk compressibility and  $\alpha$  is the constant pressure thermal expansivity of fluids.

### *Equation of state for fluid plases*

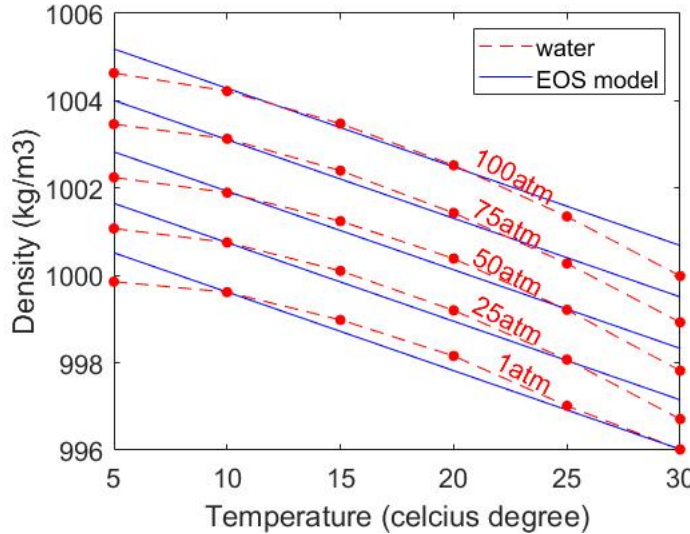


Figure 3: Equation of state of water

The equation of state establishes relations between thermodynamics variables  $[P_f, \rho_f, T_f]$ . The choice of the equation of state depends on the types of the fluid materials. For example, for the air, it is possible to assume the equation of state for the perfect gas which obeys:

$$P_f = \rho_f R T_f \quad (12)$$

where  $R$  is the gas constant. For the water, a simple linear equation of state is in the following form:

$$P_f = P_{ref} + K_f (\rho_f - \rho_{ref} - \alpha_f (T_f - T_{ref})) \quad (13)$$

where reference pressure  $P_{ref} = 1 \text{ atm} = 101325 \text{ Pa}$ , reference temperature  $T_{ref} = 10^\circ\text{C}$ , reference density  $\rho_{ref} = 999.8 \text{ kg/m}^3$ , the bulk modulus of water  $K_f = 2 \text{ GPa}$ , and the water thermal expansion  $\alpha_f = 0.18 \text{ kg/m}^3 \text{ per Celsius degree}$ . Equation (13) matches well with the state of the water (see Figure 3).

### Constitutive soil model

As a result of the explicit MPM formulation, we can derive the constitutive law in the updated Lagrangian framework of "small strain - large deformation". Therefore, the rotation of the particles (representative element volume) is manipulated by rotating the Cauchy stress tensor. First, the deformation gradient is decomposed into the polar rotation tensor  $\mathbf{R}_s^{n+1}$  and sketch tensor  $\mathbf{V}_s^{n+1}$  as

$$\mathbf{F}_s^{n+1} = \mathbf{V}_s^{n+1} \mathbf{R}_s^{n+1} \quad (14)$$

Then, before calling the constitutive model, the stress and strain rate tensor are rotated to the reference configuration as

$$\boldsymbol{\sigma}'^{n*} = (\mathbf{R}_s^{n+1})^T \boldsymbol{\sigma}'^{n*} \mathbf{R}_s^{n+1} \quad (15)$$

$$\delta\boldsymbol{\epsilon}^{n*} = (\mathbf{R}_s^{n+1})^T \delta\boldsymbol{\epsilon}_s^{n*} \mathbf{R}_s^{n+1} \quad (16)$$

Using the constitutive model with the input tensors  $\boldsymbol{\sigma}'^{n*}, \delta\boldsymbol{\epsilon}^{n*}$  to compute the Cauchy stress tensor at the advanced time step  $\boldsymbol{\sigma}'^{n+1*}$  then rotating it back to current configuration

$$\boldsymbol{\sigma}'^{n+1} = \mathbf{R}_s^{n+1} \boldsymbol{\sigma}'^{n+1*} (\mathbf{R}_s^{n+1})^T \quad (17)$$

In this paper, we adopt the hyper-elastic Neo Hookean model for the structure materials and additionally Mohr-Coulomb failure criteria for the soil (porous media) materials. The Cauchy stress of the hyper-elastic Neo Hookean model can be written as:

$$\boldsymbol{\sigma}' = \frac{\lambda \ln(J)}{J} + \frac{\mu}{J} (\mathbf{F} \mathbf{F}^T - \mathbf{J}) \quad (18)$$

where  $\lambda$  and  $\mu$  are bulk and shear modulus ad  $J$  is the determinant of the deformation gradient  $\mathbf{F}$ . And the yield function  $f$  and flow potentials  $g$  of the Mohr-Coulomb can be written as:

$$\begin{aligned} f &= \sigma'_1 - \sigma'_3 - 2c' \cos(\phi') - (\sigma'_1 + \sigma'_3) \sin(\phi') \\ g &= \sigma'_1 - \sigma'_3 - 2c' \cos(\psi') - (\sigma'_1 + \sigma'_3) \sin(\psi') \end{aligned} \quad (19)$$

where the  $c'$ ,  $\phi'$  and  $\psi'$  are cohesion and friction angle and dilation angle.  $\sigma'_1$  and  $\sigma'_3$  are maximum and minimum principal stress.

### Momentum and Energy exchange model

Currently, the energy exchange coefficient  $H_{sf}$  is assumed to be constant for the sake of simplicity. Then the energy exchange can be written as:

$$q_{sf} = H_{sf}\phi_f\phi_s(T_f - T_s) \quad (20)$$

For the momentum exchange, we assume that the drag force  $\mathbf{f}_d$  depends on the average grain size of the grains  $D_p$ , the porosity  $n$ , the fluid viscosity  $\mu_f$ , and is proportional to the relative velocities of soil grains and fluid  $(\mathbf{U}_s - \mathbf{U}_f)$ . Based on recent investigation of CFD simulations of fluid flow around mono- and bi-disperse packing of spheres for  $0.1 < \phi_s < 0.6$  and  $Re < 1000$  [19]. The drag force is given by:

$$\mathbf{f}_d = \frac{18\phi_s(1-\phi_s)\mu_f}{D_p^2} F(\phi_s, Re)(\mathbf{U}_s - \mathbf{U}_f) \quad (21)$$

where Reynolds number  $Re$  are computed as:

$$Re = \frac{n\rho_f D_p}{\mu_f} \|\mathbf{U}_s - \mathbf{U}_f\| \quad (22)$$

The function  $F(\phi_s, Re)$  can be calculated as:

$$F(\phi_s, Re) = F(\phi_s, 0) + \frac{0.413Re}{24(1-\phi_s)^2} \left( \frac{(1-\phi_s)^{-1} + 3\phi_s(1-\phi_s) + 8.4Re^{-0.343}}{1 + 10^{3\phi_s} Re^{-(1+4\phi_s)/2}} \right) \quad (23)$$

where the low Reynold coefficient  $F(\phi_s, Re \rightarrow 0)$  is:

$$F(\phi_s, 0) = \frac{10\phi_s}{(1-\phi_s)^2} + (1-\phi_s)^2(1 + 1.5\sqrt{\phi_s}) \quad (24)$$

When validating the model with analytical solution, it requires to know the hydraulic conductivity. In such case, we convert the equation (21) to Kozeny-Carman formula by assuming  $F(\phi_s, Re) = 10\phi_s/(1-\phi_s)^2$ , then the hydraulic conductivity will be expressed as  $K = D_p^2(1-\phi_s)^3/180\mu\phi_s^2$ .

### Solving momentum exchange with an implicit solve

The derivation of the implicit integration for the momentum exchange is presented in the Appendix's section 'Momentum exchange with an implicit solve'. The linear equations has the form:

$$\begin{vmatrix} (1+\beta_{12}) & -\beta_{12} \\ -\beta_{21} & (1+\beta_{21}) \end{vmatrix} \begin{vmatrix} \Delta\mathbf{U}_f \\ \Delta\mathbf{U}_s \end{vmatrix} = \begin{vmatrix} \beta_{12}(\mathbf{U}_s^* - \mathbf{U}_f^*) \\ \beta_{21}(\mathbf{U}_f^* - \mathbf{U}_s^*) \end{vmatrix}$$

where the intermediate velocity can be calculated by

$$\begin{aligned}\mathbf{U}_f^* &= \mathbf{U}_f^n + \Delta t \left( -\frac{\nabla P_f^{n+1}}{\rho_f^n} + \frac{\nabla \cdot \boldsymbol{\tau}_f^n}{\bar{\rho}_f^n} + \mathbf{b} \right) \\ \mathbf{U}_s^* &= \mathbf{U}_s^n + \Delta t \left( \frac{\nabla \cdot \boldsymbol{\sigma}'^n}{\bar{\rho}_s^n} - \frac{\nabla P_f^{n+1}}{\rho_s} + \mathbf{b} \right)\end{aligned}\quad (25)$$

Also, the momentum exchange coefficient can be computed at every time step as  $\beta_{12} = K/\bar{\rho}_f^n$  and  $\beta_{21} = K/\bar{\rho}_s^n$  with the coefficient  $K = 18\phi_s(1 - \phi_s)\mu_f F(\phi_s, Re)/D_p^2$ .

#### *Turbulent model*

The turbulent effect is modelled using a statistical approach namely large-eddy simulation. In this approach, the micro-scale turbulent influence in the dynamics of the macro-scale motion is computed through simple models like Smagorinsky model. In the Smagorinsky mode, the residual stress tensor is:

$$\tau_{ij} = 2\mu_{eff}(\bar{S}_{ij} - \frac{1}{3}\delta_{ij}\bar{S}_{kk}) + \frac{1}{3}\delta_{ij}\tau_{kk} \quad (26)$$

where the strain rate tensor is given by

$$\bar{S}_{ij} = \frac{1}{2} \left( \frac{\delta \bar{\mathbf{U}}_i}{\delta x_j} + \frac{\delta \bar{\mathbf{U}}_j}{\delta x_i} \right) \quad (27)$$

and the effective viscosity is sum of molecular viscosity and turbulent viscosity  $\mu_{eff} = \mu + \mu_t$  in which the turbulent viscosity  $\mu_t$  is calculated by

$$\mu_t = (C_s \Delta)^2 \sqrt{2\bar{S}_{ij}\bar{S}_{ij}} \quad (28)$$

where  $C_s$  is the Smagorinsky constant and  $\Delta = \sqrt[3]{dx dy dz}$  is the grid size that defines the subgrid length scale.

#### *Contact law for soil-structure interaction*

MPMICE includes a contact law for the interaction between soil and structure using the first Coulomb friction contact for MPM presented by Bardenhagen et al. ([20]). The magnitude of the friction force at the contact depends on the friction coefficient  $\mu_{fric}$  and the normal force  $f_{norm}$  computed from the projection of the contact force in the normal direction.

$$f_{fric} = \mu_{fric} f_{norm} \quad (29)$$

The contact determines whether the soil is sliding or sticking to the structure by comparing the friction force with the sticking force  $f_{stick}$  computed from the projection of the contact force in the tangent direction:

$$\begin{aligned} & \text{if } f_{fric} \geq f_{stick} \text{ no sliding} \\ & \text{if } f_{fric} < f_{stick} \text{ sliding occurs} \end{aligned} \quad (30)$$

## Numerical implementation

The fluid phase is discretized in the grid with the state variables stored at the centroid of the cells  $[\rho_{fc}, \mathbf{U}_{fc}, T_{fc}, v_{fc}]$  while the solid phase is discretized in the particles with the state variables  $[m_{sp}, \mathbf{U}_{sp}, T_{sp}, \boldsymbol{\sigma}'_{sp}]$ . The time discretization are solved using the following steps:

### *Interpolation from Solid Particle to Grid*

The nodal values of the solid state (mass, velocity, temperature, volume) are:

$$\begin{aligned} m_{si}^n &= \sum S_{ip} m_{sp} \\ \mathbf{U}_{si}^n &= \frac{\sum S_{ip} (m\mathbf{U})_{sp}^n}{m_{si}^n} \\ T_{si}^n &= \frac{\sum S_{ip} (mT)_{sp}^n}{m_{si}^n} \\ V_{si}^n &= \frac{\sum S_{ip} (mV)_{sp}^n}{m_{si}^n} \\ \boldsymbol{\sigma}_{si}^n &= \frac{\sum S_{ip} (\boldsymbol{\sigma}V)_{sp}^n}{V_{si}^n} \end{aligned} \quad (31)$$

The nodal internal forces is calculated by

$$\mathbf{f}_{si}^{int,n} = - \sum \nabla S_{ip} (\boldsymbol{\sigma}'_{sp})^n V_{sp}^n \quad (32)$$

The nodal external forces  $\mathbf{f}_{si}^{ext,n}$  and extra momentum from contact forces are computed here. The nodal velocity and nodal temperature are applied boundary conditions.

Then we compute the solid cell variables as:

$$\begin{aligned}
m_{sc}^n &= \sum S_{ci} m_{si} \\
\rho_{sc}^n &= \frac{m_{sc}^n}{V} \\
\mathbf{U}_{sc}^n &= \sum S_{ci} \mathbf{U}_{si}^n \\
T_{sc}^n &= \sum S_{ci} T_{si}^n \\
V_{sc}^n &= \sum S_{ci} V_{si}^n \\
\boldsymbol{\sigma}_{sc}^n &= \sum S_{ci} \boldsymbol{\sigma}_{si}^n
\end{aligned} \tag{33}$$

#### *Compute equation of state for fluid phase*

Considering the total fluid material volume of a cell is:

$$V_{total} = \sum_{f=1}^{N_f} M_f v_f \tag{34}$$

Then we need to find  $P_{eq}$  which allows each fluid materials obey their equation of states  $[P_f, \rho_f, v_f, T_f, e_f]$  but also allow mass of all fluid materials to fill the entire the pore volume without ongoing compression or expansion following the condition:

$$0 = n - \sum_{f=1}^{N_f} v_f \rho_f \tag{35}$$

Then, we can use he Newton-Raphson interation to find the value of  $P_{eq}$  which satisfies the equation (34, 35) and each equation of states of each fluid materials.

#### *Compute faced-centered velocity*

Following the derivation in the Appendix: Advanced Fluid Pressure, we first compute the fluid face-centered velocity as

$$\mathbf{U}_{f,FC}^* = \frac{(\bar{\rho} \mathbf{U})_{f,FC}^n}{\bar{\rho}_{f,FC}^n} + \Delta t \left( -\frac{\nabla^{FC} P_{eq}}{\bar{\rho}_{f,FC}^n} + \frac{\nabla^{FC} \cdot \boldsymbol{\tau}^n}{\bar{\rho}_{s,FC}} + \mathbf{b} \right) \tag{36}$$

The equation (36) is discretized in three dimension (noted that  $\nabla^{FC} \cdot \boldsymbol{\tau} = 0$ ), for example the discretized equation in the x direction is

$$U_{fx}^* = \frac{(\bar{\rho}U)_{fx,R}^n + (\bar{\rho}U)_{fx,L}^n}{\bar{\rho}_{fx,L}^n + \bar{\rho}_{fx,R}^n} + \Delta t \left( -\frac{2(v_{fx,L}^n v_{fx,R}^n)}{v_{fx,L}^n + v_{fx,R}^n} \frac{P_{eqx,R} - P_{eqx,L}}{\Delta x} + b_x \right) \quad (37)$$

The face-centered solid velocity can be calculated as

$$\mathbf{U}_{s,FC}^* = \frac{(\bar{\rho}\mathbf{U})_{s,FC}^n}{\bar{\rho}_{s,FC}^n} + \Delta t \left( \frac{\nabla^{FC} \cdot \boldsymbol{\sigma}_c'^n}{\bar{\rho}_{s,FC}} - \frac{\nabla^{FC} P_{eq}}{\rho_s} + \mathbf{b} \right) \quad (38)$$

The equation (38) is discretized in three dimension(noted that  $\nabla^{FC} \cdot \sigma_{ij} = 0$  with  $i \neq j$ ), for example the discretized equation in the x direction is

$$U_{sx}^* = \frac{(\bar{\rho}U)_{sx,R}^n + (\bar{\rho}U)_{sx,L}^n}{\bar{\rho}_{sx,L}^n + \bar{\rho}_{sx,R}^n} + \Delta t \left( \frac{2(\sigma_{xx,R} - \sigma_{xx,L})}{(\bar{\rho}_{sx,L}^n + \bar{\rho}_{sx,R}^n)\Delta x} - \frac{P_{eqx,R} - P_{eqx,L}}{\rho_s \Delta x} + b_x \right) \quad (39)$$

Computing the modified faced-centered velocity  $\mathbf{U}_{FC}^L$  considering the momentum exchange

$$\begin{aligned} \mathbf{U}_{f,FC}^L &= \mathbf{U}_{f,FC}^* + \Delta \mathbf{U}_{f,FC} \\ \mathbf{U}_{s,FC}^L &= \mathbf{U}_{s,FC}^* + \Delta \mathbf{U}_{s,FC} \end{aligned} \quad (40)$$

By solving the linear equation below to obtain the increment of velocity

$$\begin{vmatrix} (1 + \beta_{12,FC}) & -\beta_{12,FC} \\ -\beta_{21,FC} & (1 + \beta_{21,FC}) \end{vmatrix} \begin{vmatrix} \Delta \mathbf{U}_{f,FC} \\ \Delta \mathbf{U}_{s,FC} \end{vmatrix} = \begin{vmatrix} \beta_{12,FC} (\mathbf{U}_{s,FC}^* - \mathbf{U}_{f,FC}^*) \\ \beta_{21,FC} (\mathbf{U}_{f,FC}^* - \mathbf{U}_{s,FC}^*) \end{vmatrix}$$

#### *Compute advanced fluid pressure (implicit scheme)*

We solve the generalized Poisson's equation below by employing a pre-conditioned conjugate gradient technique with a multi-grid pre-conditioner

$$\left( \kappa - \nabla^c \frac{\Delta t}{\bar{\rho}_{f,FC}} \cdot \nabla^{FC} \right) \Delta P_c^n = -\nabla^c \cdot \mathbf{U}_{f,FC}^L \quad (41)$$

The advanced fluid pressure at cell center is

$$P_c^{n+1} = P_{eq} + \Delta P_c^n \quad (42)$$

Finally, the faced-centered advanced fluid pressure is

$$P_{f,FC}^{n+1} = \left( \frac{P_{f,L}^{n+1}}{\bar{\rho}_{f,L}^n} + \frac{P_{f,R}^{n+1}}{\bar{\rho}_{f,R}^n} \right) / \left( \frac{1}{\bar{\rho}_{f,L}^n} + \frac{1}{\bar{\rho}_{f,R}^n} \right) = \left( \frac{P_{f,L}^{n+1} \bar{\rho}_{f,R}^n + P_{f,R}^{n+1} \bar{\rho}_{f,L}^n}{\bar{\rho}_{f,L}^n \bar{\rho}_{f,R}^n} \right) \quad (43)$$

### *Compute viscous shear stress term of the fluid phase*

This part compute the viscous shear stress  $\Delta(m\mathbf{U})_{fc,\tau}$  for a single viscous compressible Newtonian fluid and optionally shear stress induced by the turbulent model.

### *Compute nodal internal temperature of the solid phase*

The nodal internal temperature rate is computed based on the heat conduction model

$$dT_{si}^L = \frac{(\Delta W_{si}^n + \nabla^i \cdot \mathbf{q}_{si}^n)}{m_{si}^n} \quad (44)$$

where  $\Delta W_{si}^n = \boldsymbol{\sigma}' : \nabla \mathbf{U}_s$  is the mechanical work rate computed from the constitutive model. The nodal internal temperature is calculated by

$$T_{si}^L = T_{si}^n + dT_{si}^L \quad (45)$$

### *Compute and integrate acceleration of the solid phase*

After interpolating from material points to the nodes, the nodal acceleration and velocity are calculate by

$$\mathbf{a}_{si}^{L-} = \frac{\mathbf{f}_{si}^{int,n} + \mathbf{f}_{si}^{ext,n}}{m_{si}^n} + \mathbf{g} \quad (46)$$

$$\mathbf{U}_{si}^{L-} = \mathbf{U}_{si}^n + \mathbf{a}_{si}^{L-} \Delta t \quad (47)$$

### *Compute Lagrangian value (mass, momentum and energy)*

For the fluid phase, the linear momentum rate, the energy rate are

$$\Delta(m\mathbf{U})_{fc} = V n_c^n \nabla^c P_{fc}^{n+1} + \Delta(m\mathbf{U})_{fc,\tau} + V \bar{\rho}_{fc}^n g \quad (48)$$

$$\Delta(me)_{fc} = V n_c^n P_{fc}^{n+1} \nabla^c \cdot \mathbf{U}_{f,FC}^* + \nabla^c \cdot \mathbf{q}_{fc}^n \quad (49)$$

The Lagrangian value of the mass, linear momentum and energy of fluid phase without momentum exchange are

$$m_{fc}^L = V \bar{\rho}_{fc}^n \quad (50)$$

$$(m\mathbf{U})_{fc}^{L-} = V \bar{\rho}_{fc}^n \mathbf{U}_{fc}^n + \Delta(m\mathbf{U})_{fc} \quad (51)$$

$$(me)_{fc}^{L-} = V \bar{\rho}_{fc}^n T_{fc}^n c_v + \Delta(me)_{fc} \quad (52)$$

For the solid phase, the Lagrangian value of the linear momentum and energy of solid phase are

$$m_{sc}^L = m_{sc}^n \quad (53)$$

$$(m\mathbf{U})_{sc}^{L-} = \sum S_{ci} m_{si}^n \mathbf{U}_{si}^{L-} + V(1 - n_c^n) \nabla^c P_{fc}^{n+1} \quad (54)$$

$$(me)_{sc}^{L-} = \sum S_{ci} m_{si}^n T_{si}^L \quad (55)$$

To consider the momentum exchange, the Lagrangian velocity is modified as

$$\begin{aligned} \mathbf{U}_{fc}^L &= \mathbf{U}_{fc}^{L-} + \Delta \mathbf{U}_{fc} \\ \mathbf{U}_{sc}^L &= \mathbf{U}_{sc}^{L-} + \Delta \mathbf{U}_{sc} \end{aligned} \quad (56)$$

where the cell-centered intermediate velocity can be calculated by

$$\begin{aligned} \mathbf{U}_{fc}^{L-} &= \frac{(m\mathbf{U})_{fc}^{L-}}{m_{fc}^L} \\ \mathbf{U}_{sc}^{L-} &= \frac{(m\mathbf{U})_{sc}^{L-}}{m_{sc}^L} \end{aligned} \quad (57)$$

And the increment of the velocity can be computed by solving the linear equation below

$$\begin{vmatrix} (1 + \beta_{12,c}) & -\beta_{12,c} \\ -\beta_{21,c} & (1 + \beta_{21,c}) \end{vmatrix} \begin{vmatrix} \Delta \mathbf{U}_{fc} \\ \Delta \mathbf{U}_{sc} \end{vmatrix} = \begin{vmatrix} \beta_{12,c} (\mathbf{U}_{sc}^{L-} - \mathbf{U}_{fc}^{L-}) \\ \beta_{21,c} (\mathbf{U}_{fc}^{L-} - \mathbf{U}_{sc}^{L-}) \end{vmatrix}$$

Finally, we obtain the cell-centered solid acceleration and temperature rate as

$$d\mathbf{U}_{sc}^L = \frac{(m\mathbf{U})_{sc}^L - (m\mathbf{U})_{sc}^n}{m_{sc}^L \Delta t} \quad (58)$$

$$dT_{sc}^L = \frac{(me)_{sc}^L - (me)_{sc}^n}{m_{sc}^L c_v \Delta t} \quad (59)$$

#### *Compute Lagrangian specific volume of the fluid phase*

To compute the Lagrangian value of the specific volume of the fluid phase, we need to compute the Lagrangian temperature rate as below

$$T_{fc}^{n+1} = \frac{(me)_{fc}^L}{m_{fc}^L c_v} \quad (60)$$

$$\frac{D_f T_{fc}}{Dt} = \frac{T_{fc}^{n+1} - T_{fc}^n}{\Delta t} \quad (61)$$

As such, the Lagrangian specific volume rate is:

$$\Delta(mv)_{fc} == V f_{fc}^\phi \nabla \cdot \mathbf{U} + (\phi_{fc} \alpha_{fc} \frac{D_f T_{fc}}{Dt} - f_{fc}^\phi \sum_{n=1}^N \phi_{nc} \alpha_{nc} \frac{D_n T_{nc}}{Dt}) \quad (62)$$

where  $f_f^\phi = (\phi_f \kappa_f) / (\sum_{n=1}^N \phi_n \kappa_n)$  and  $\mathbf{U} = \nabla \cdot (\sum_{s=1}^{N_s} \phi_{sc} \mathbf{U}_{sc} + \sum_{f=1}^{N_f} \phi_{fc} \mathbf{U}_{fc})$ . Finally, the Lagrangian specific volume is

$$(mv)_{fc}^L = V \bar{\rho}_{f,c}^n v_{fc}^n + \Delta(mv)_{fc} \quad (63)$$

#### *Compute advection term and advance in time*

The time advanced mass, linear momentum, energy and specific volume are:

$$m_{fc}^{n+1} = m_{fc}^L - \Delta t \text{Advection}(\bar{\rho}_{fc}^L, \mathbf{U}_{f,FC}^L) \quad (64)$$

$$(m\mathbf{U})_{fc}^{n+1} = (m\mathbf{U})_{fc}^L - \Delta t \text{Advection}((\bar{\rho}\mathbf{U})_{fc}^L, \mathbf{U}_{f,FC}^L) \quad (65)$$

$$(me)_{fc}^{n+1} = (me)_{fc}^L - \Delta t \text{Advection}((\bar{\rho}c_v T)_{fc}^L, \mathbf{U}_{f,FC}^L) \quad (66)$$

$$(mv)_{fc}^{n+1} = (mv)_{fc}^L - \Delta t \text{Advection}((\bar{\rho}v)_{fc}^L, \mathbf{U}_{f,FC}^L) \quad (67)$$

Finally, the state variables of the fluid phase of the next time step are

$$\bar{\rho}_{fc}^{n+1} = \frac{m_{fc}^{n+1}}{V} \quad (68)$$

$$\mathbf{U}_{fc}^{n+1} = \frac{(m\mathbf{U})_{fc}^{n+1}}{m_{fc}^{n+1}} \quad (69)$$

$$T_{fc}^{n+1} = \frac{(me)_{fc}^{n+1}}{m_{fc}^{n+1}} \quad (70)$$

$$v_{fc}^{n+1} = \frac{(mv)_{fc}^{n+1}}{m_{fc}^{n+1}} \quad (71)$$

### *Interpolate from cell to node of the solid phase*

First we interpolate the acceleration, velocity and temperature to the node

$$\mathbf{a}_{si}^n = \sum S_{ci} d\mathbf{U}_{sc}^L \quad (72)$$

$$\mathbf{U}_{si}^{n+1} = \sum S_{ci} d\mathbf{U}_{sc}^L \Delta t \quad (73)$$

$$dT_{si}^n = \sum S_{ci} dT_{sc}^L \quad (74)$$

Then the boundary condition and contact forces are applied to the nodal velocity and the acceleration is modified by

$$\mathbf{a}_{si}^n = \frac{\mathbf{v}_{si}^{n+1} - \mathbf{v}_{si}^n}{\Delta t} \quad (75)$$

### *Update the particle variables*

The state variables of the solid phase  $[\mathbf{U}_{sp}^{n+1}, \mathbf{x}_{sp}^{n+1}, \nabla \mathbf{U}_{sp}^{n+1}, T_{sp}^{n+1}, \mathbf{F}_{sp}^{n+1}, V_{sp}^{n+1}]$  (velocity, position, velocity gradient, temperature, deformation gradient, volume) are updated here

$$\mathbf{U}_{sp}^{n+1} = \mathbf{U}_{sp}^n + \sum S_{sp} \mathbf{a}_{si}^n \Delta t \quad (76)$$

$$\mathbf{x}_{sp}^{n+1} = \mathbf{x}_{sp}^n + \sum S_{sp} \mathbf{U}_{si}^{n+1} \Delta t \quad (77)$$

$$\nabla \mathbf{U}_{sp}^{n+1} = \sum \nabla S_{sp} \mathbf{U}_{si}^{n+1} \quad (78)$$

$$T_{sp}^{n+1} = T_{sp}^n + \sum S_{sp} dT_{si}^n \Delta t \quad (79)$$

$$\mathbf{F}_{sp}^{n+1} = (\mathbf{I} + \nabla \mathbf{U}_{sp}^{n+1} \Delta t) \mathbf{F}_{sp}^n \quad (80)$$

$$V_{sp}^{n+1} = \det(\mathbf{F}_{sp}^{n+1}) V_{sp}^o \quad (81)$$

Finally, the effective stress  $(\sigma')^{n+1}$  is updated from the constitutive model.

## Numerical examples

All input files and the analytical calculations in this section are provided in the Github repository <sup>1</sup> for the reproduction of the numerical results.

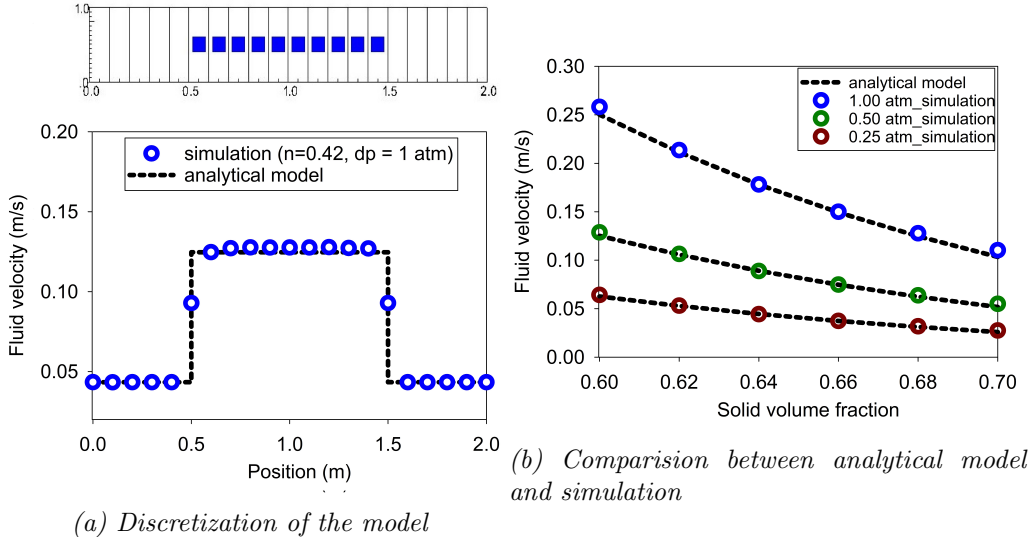


Figure 4: Numerical results of the fluid flow through isothermal porous media

### Fluid Flow through isothermal porous media

Fluid flow through porous media is important in many engineering disciplines, like predicting water flow in soil. Fluid flow velocity in one dimension can be calculated from the porous media's hydraulic conductivity  $K$  as:

$$U_f = K \frac{\Delta p_f}{L} \quad (82)$$

If the Carman-Kozeny formula is adopted  $F = 10\phi_s/(1 - \phi_s)^2$ , the hydraulic conductivity will be expressed as  $K = d^2(1 - \phi_s)^3/180\mu\phi_s^2$ . Then, the analytical formula of average velocity in one dimension through the porous media is:

$$U_f = \frac{1}{n} \frac{d^2(1 - \phi_s)^3}{180\mu\phi_s^2} \frac{\Delta p_f}{L} \quad (83)$$

Our numerical model is validated by modeling fluid flow through a 1m long porous media. This fluid has water properties (bulk modulus is 2GPa, density is 998 kg/m<sup>3</sup> at 5 degrees Celsius and 10325 Pa (1atm) pressure, dynamic viscosity  $\mu$  is 1mPa s). The porous media is modeled by elastic material with Young's modulus is 10 MPa, Poisson's ratio is 0.3, and density

---

<sup>1</sup>[https://github.com/QuocAnh90/Uintah\\_NTNU](https://github.com/QuocAnh90/Uintah_NTNU)

is 2650 kg/m<sup>3</sup>. The volume fraction of porous media  $\phi_s$  is [0.6, 0.62, 0.66, 0.68, 0.7] and the average grain diameter  $d$  is 1mm. The model is discretized in 20 finite element and the porous media in 10 finite element with 1 material point per element. The pressure gradient is applied with three different value [0.25, 0.5, 1] atm. Figure 4 shows a good agreement of fluid flow prediction between the theory and the model.

### Isothermal consolidation

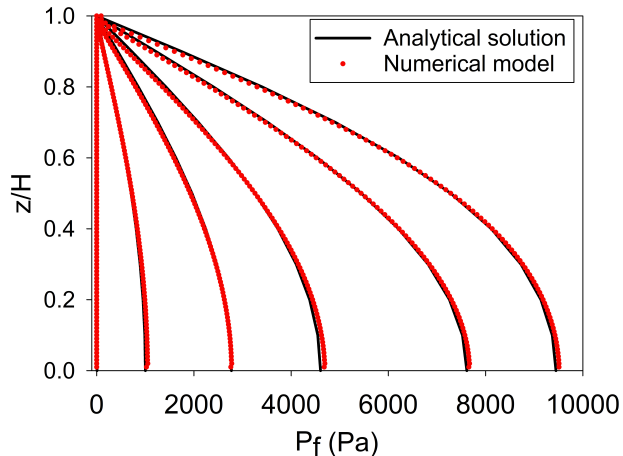


Figure 5: Comparison between analytical solution and numerical solution

A common benchmark for a fully saturated porous media is the simulation of one-dimensional consolidation. Using the Carman-Kozeny formula, the time-dependent pressure can be calculated as:

$$p_f = \sum_{m=1}^{\infty} \frac{2F_{ext}}{M} \sin\left(\frac{Mz}{H}\right) e^{-M^2 T_v} \text{ with } M = \frac{\pi}{2}(2m+1) \quad (84)$$

where the consolidation rate  $T_v = C_v t / H^2$ , the consolidation coefficient  $C_v = E_v n^3 d^2 / (180(1-n)^2 \mu)$  and the Oedometer modulus  $E_v = E(1-\nu)/(1+\nu)/(1-2\nu)$ . Our numerical model is validated by modeling the consolidation of a 1m column. This fluid has water properties (bulk modulus is 2GPa, density is 998 kg/m<sup>3</sup> at 5 degrees Celsius and 10325 Pa (1atm) pressure, dynamic viscosity  $\mu$  is 1mPa s). The porous media is modeled by elastic

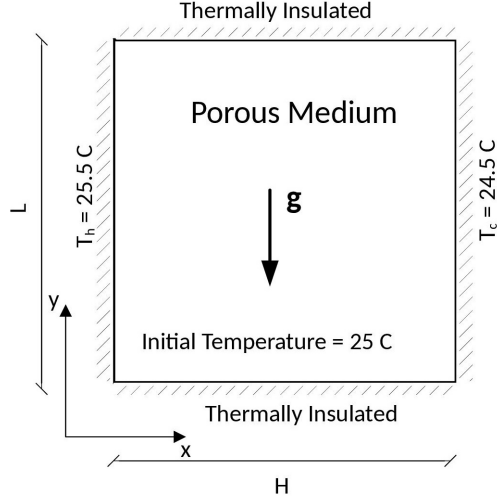


Figure 6: Model schematic

material with Young's modulus is 10 MPa, Poisson's ratio is 0.3, and density is 2650 kg/m<sup>3</sup>. The volume fraction of porous media  $\phi_s$  is 0.7 which is equivalent to the porosity of 0.3 and the average grain diameter  $d$  is 1mm. The model is discretized in 100 finite element with 1 material point per element. The external pressure applies to the top of the column is 10 kPa. Figure 5 shows a good agreement of fluid flow prediction between the theory and the model.

#### *Thermal induced cavity flow*

Another benchmark is the thermal induced cavity flow in porous media. Temperature and velocity distributions are calculated for a square non-deformable saturated porous media. The top and bottom walls are insulated, and the left and right walls are at fixed temperatures differing by 1 C. The fluid motion at steady state are cavity flow due to the temperature induced density variation.

The numerical is validated by comparing with the numerical solution of the finite element method. The fluid has water properties (bulk modulus is 2GPa, density is 998 kg/m<sup>3</sup> at 5 degrees Celsius and 10325 Pa (1atm) pressure, dynamic viscosity  $\mu$  is 1 mPa s). The porous media is modeled by non deformable material, and density is 2500 kg/m<sup>3</sup>. The specific heat capacity

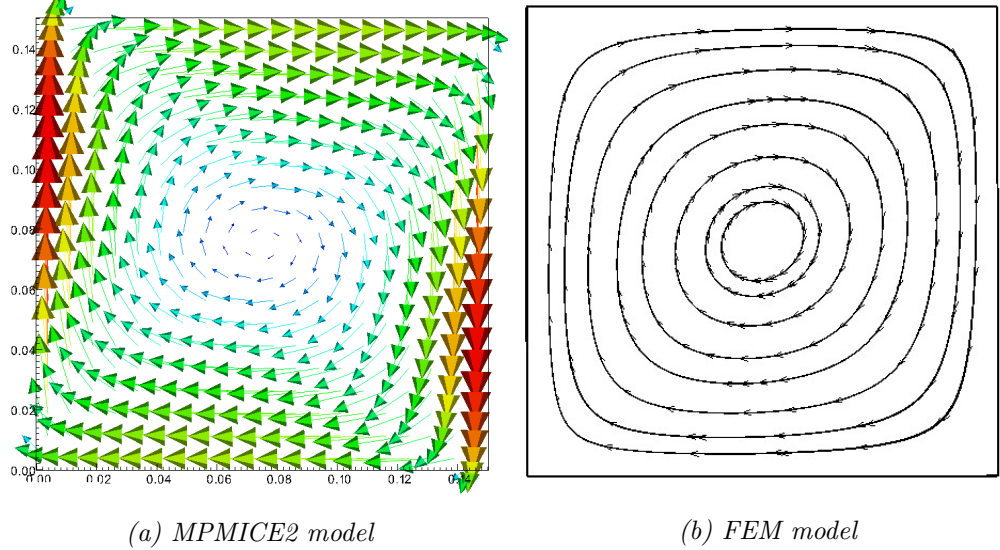


*Figure 7: Comparision between MPMICE2 model and FEM model*

of the water and porous skeleton are 4181 J/kg.K and 835 J/kg.K respectively. The thermal conductivity of the water and porous skeleton are 0.598 W/m.K and 0.4 W/m.K. The volume fraction of porous media  $\phi_s$  is 0.6 which is equivalent to the porosity of 0.4 and the average grain diameter  $d$  is 1mm. The model is discretized in 20 x 20 finite element with 4 material point per element. Figure 7 shows a good agreement of numerical results of the model compared with the numerical solution of the finite element method.

#### *Underwater debris flow*

The numerical example is validated by Rzadkiewicz et al.'s experiment on submarine debris flow [21]. During the experiment, sand in a triangular box is released and then slides along a rigid bed inclined 45 degrees under water, see Figure 8.

In the numerical model, the material properties are selected based on the experiment by Rzadkiewicz et al [21]. Sand has a saturated density of 1985 kg/m<sup>3</sup> and yield stress of 200 Pa. Young's modulus has little effect on debris flow run-out because of the extreme large deformation of the debris. Therefore, we select 50 MPa Young's modulus with 0.25 Poisson's ratio. The rigid bed is much stiffer with bulk modulus and shear modulus of  $117e^7$  Pa and

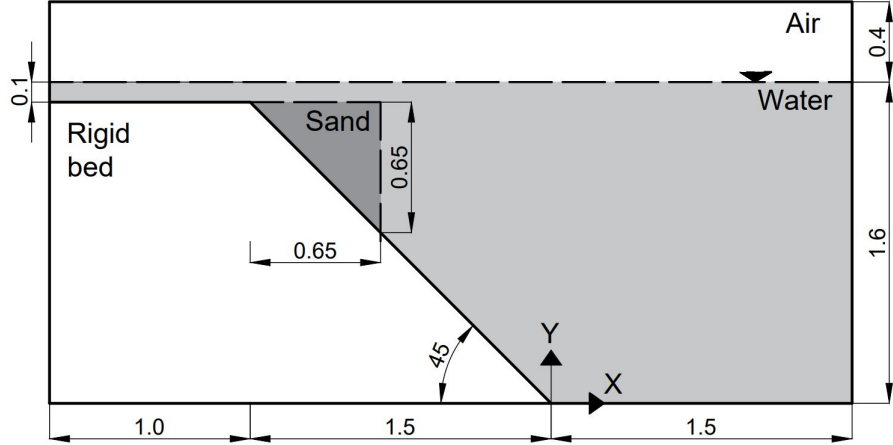


Figure 8: Model schematic

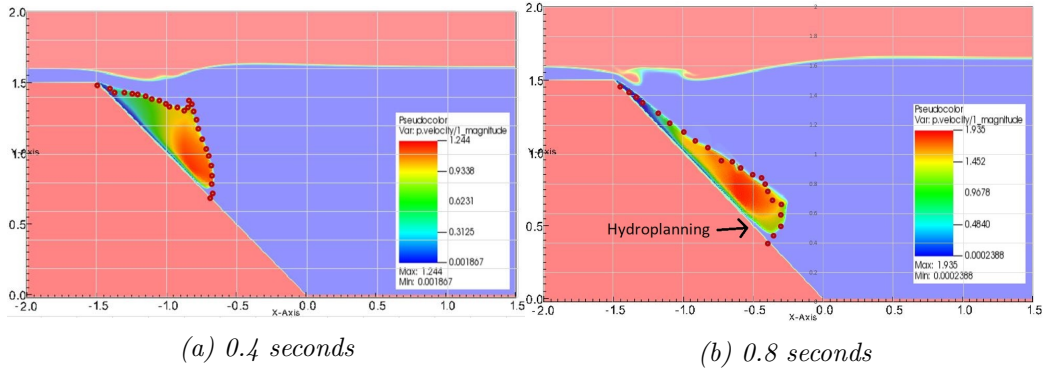


Figure 9: Simulation of underwater debris flow

$43.8e^7$  Pa. Under gravity, the density of the water at the surface is  $999.8 \text{ kg/m}^3$  at the pressure of 1 atm. At the top boundary, the air has a density of  $1.17 \text{ kg/m}^3$  at the atmospheric pressure of 1 atm. At 5 Celcius degrees, air and water have viscosity of  $18.45e^{-3}$  mPa s and 1 mPa s respectively. The numerical parameters used in this example are presented in Table 2.

On all boundary faces, the Dirichlet boundary condition is imposed for velocity ( $u = 0 \text{ m/s}$ ) and temperature ( $T = 5 \text{ Celcius degrees}$ ), while the Neuman boundary condition is imposed at the top boundary for pressure ( $dp/dx = 0 \text{ kPa}$ ) and density ( $d/dx = 0 \text{ kg/m}^3$ ). For the background mesh, there are  $700 \times 400 = 280.000$  cells. In each cell of the debris flow and rigid bed, there are  $2 \times 2$  material points.

Materials	Bulk modul (Pa)	Shear modul (Pa)	Density (kg/m3)	Temp (C)	Dynamic viscosity (Pa s)	Yield stress (Pa)
Water (at surface)	2.15e9	-	999.8	5	855e-6	-
Air (at top boundary)	-	-	1.177	5	18.45e-6	-
Sand (porous media)	8.33e6	20e6	1985	5	-	200
Rigid bed (solid)	117e7	43.8e7	8900	5	-	-

Table 2: Numerical parameters for the underwater submarine debris

Figure 9a and 9b show snapshots of the debris flow sliding in the plane at 0.4 s and 0.8 s. Our simulations match the computed results from Rzadkiewicz et al. [21]. The model also captures typical hydroplaning mechanism of the underwater debris flow (hydroplaning means the debris flow is lifted up and no longer in contact with the bottom layer). The elevation of the free surface at 0.4s and 0.8s is compared between our proposed method and other methods in Figure 10. Once again, our computed results were consistent with both the experiment and others computational results [7]. Unlike other computational models based on total stress analysis, the proposed model based on the effective stress analysis which allows to analyze the water pressure and temperature in the debris flow.

We also explore the difference between underwater debris flow and saturated debris flow in terms of interacting with obstacle. Figure 11 shows the snapshot of the simulations of underwater and saturated debris flow. The saturated debris flow (see Figure 11a) behaves like frictional flow as grain have contact forces with each other. On the other hand, the underwater debris flow (see Figure 11b) behaves like turbulent flow as grains are separated from each other and exhibit no contact forces between grains.

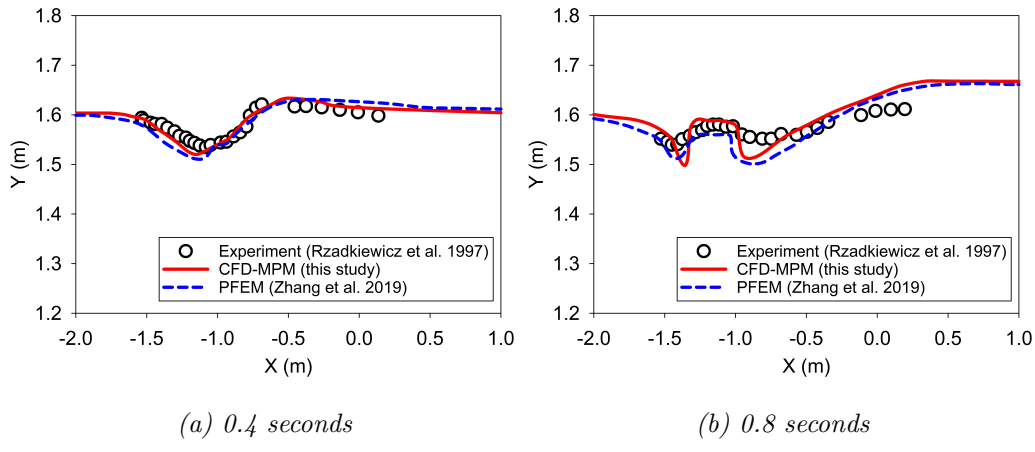


Figure 10: Simulation of underwater debris flow

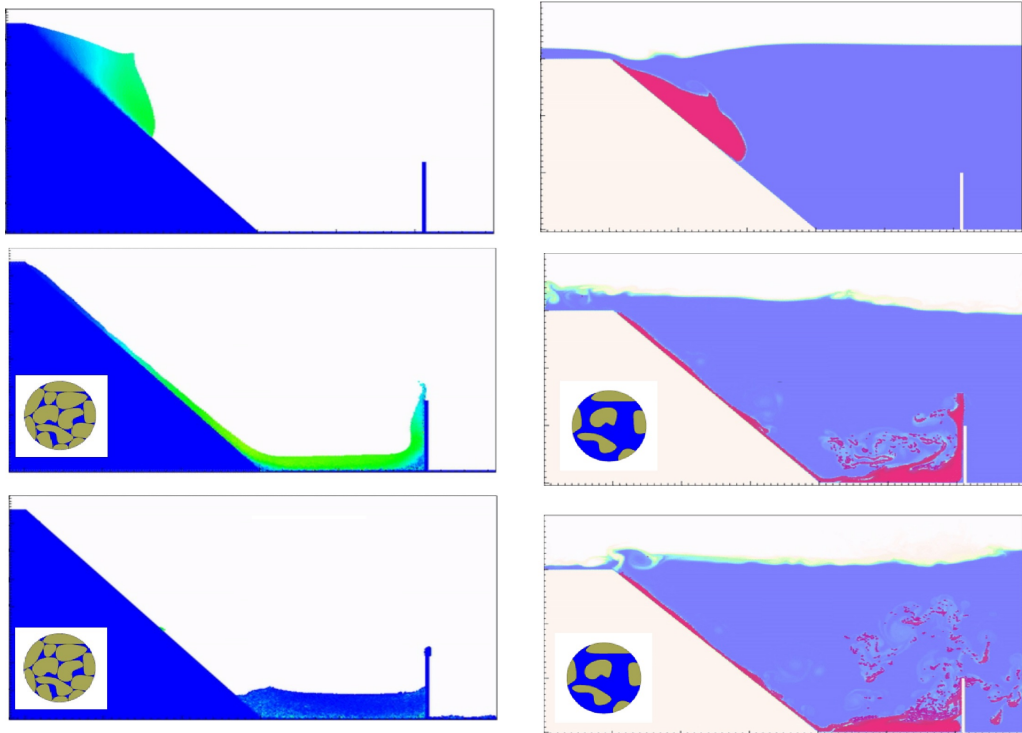


Figure 11: Simulation of underwater debris flow

### Earthquake-induced submarine landslides

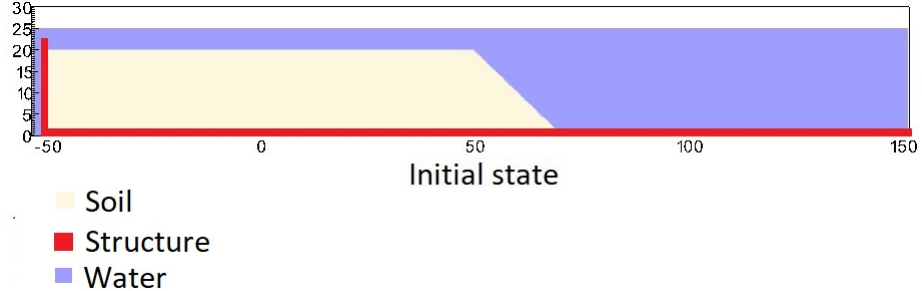


Figure 12: Numerical model of the earthquake-induced submarine landslide

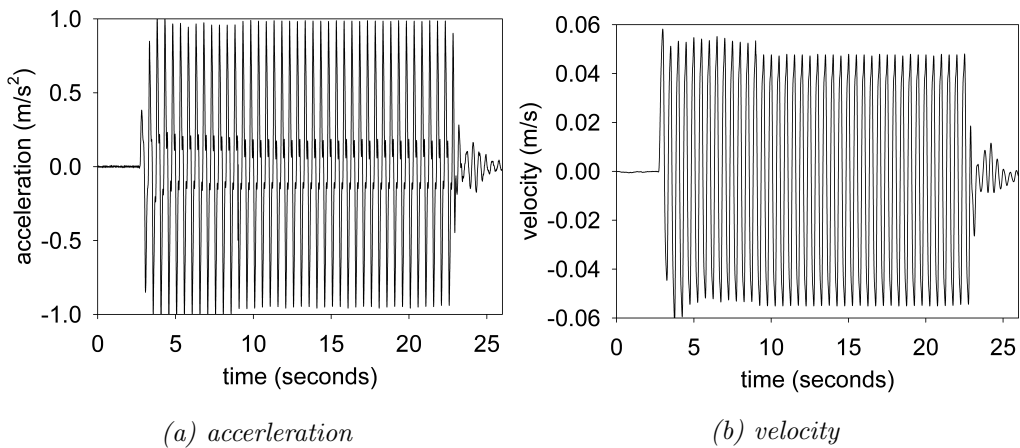


Figure 13: Ground acceleration profile, frequency of 2Hz and magnitude of 1g

In the final example, we perform numerical analysis of the earthquake induced submarine landslides. A plane strain model with the slope under water is shown in Figure 12. A slope underwater is placed in a horizontal and vertical structure which was used to be a skaing table to apply earthquake loading. We simplify the earthquake loading by simulating the ground shaking for 20 seconds with the peak ground acceleration of 1g and the frequency of 2Hz (see Figure 13a). The ground motion is applied in terms of velocity (see Figure 13b). The earthquake of this magnitude can occured typically for the earthquake of magnitude of more than 6.

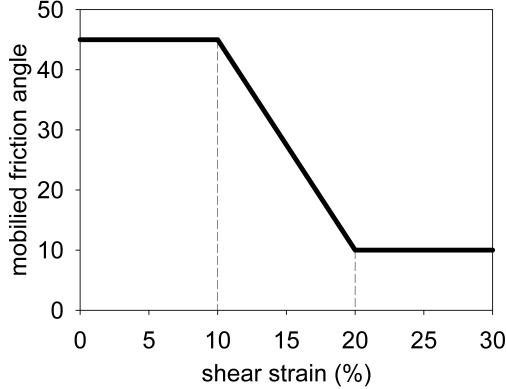
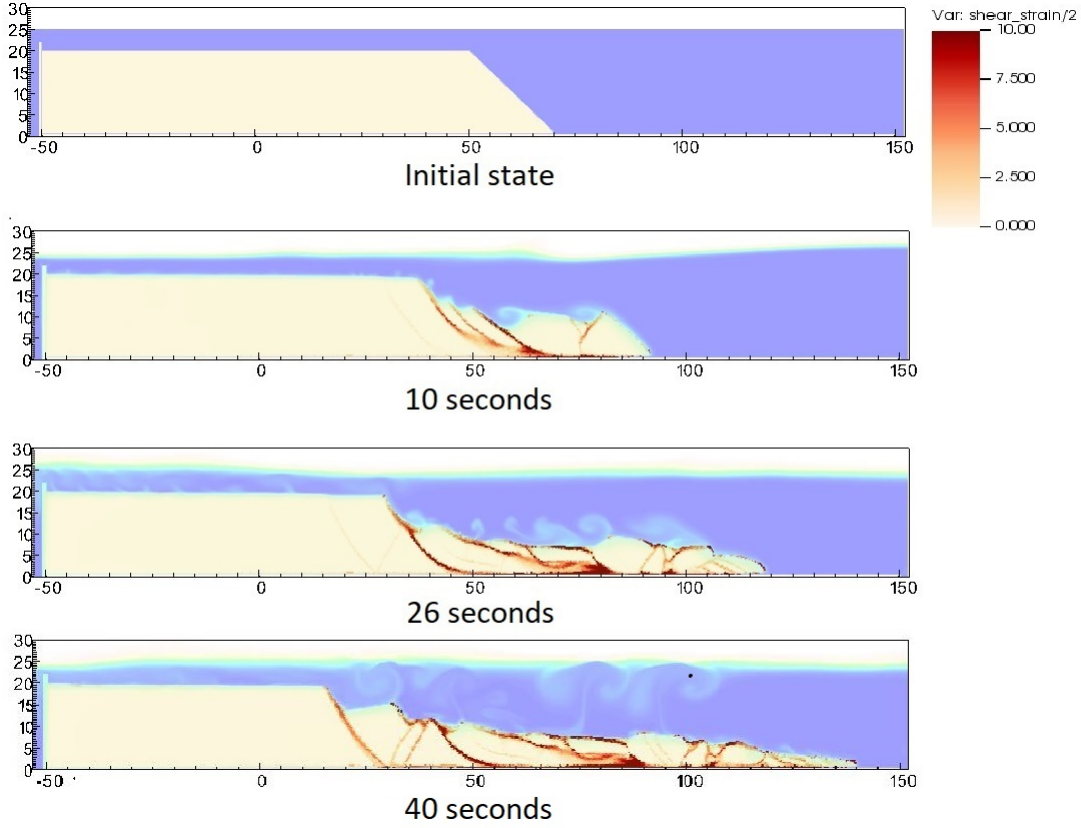


Figure 14: Mobilized friction angle in Mohr Coulomb model

A non-associated Mohr-Coulomb model is used for the sand. The soil grain has the density of  $2650 \text{ kg/m}^3$ , Young's modulus of  $10 \text{ kPa}$  and Poisson's ratio of  $0.3$  and zero cohesion. The friction angle is mobilized following the softening curve (see Figure 14) with the peak friction angle of  $45$  degrees and the residual friction angle of  $10$  degrees. The average grain size of the clay is around  $0.1 \mu\text{m}$  to mimic the undrained behavior. The mobilized dilatancy angle is calculated from the Row-stress dilatancy as follow:

$$\sin \psi_m = \frac{\sin \phi_m}{\sin \psi_{cs}(1 - \sin \phi_m)} \quad (85)$$

The solid plane is modeled as a rigid body acted as a shaking table. The contact between horizontal plane and the sand is the frictional contact with the friction coefficient of  $0.1$ . No artificial damping is applied in the simulation. The contact between vertical plane and the sand is considered to be smooth with zero friction coefficient. Under gravity, the density of the water at the surface is  $999.8 \text{ kg/m}^3$  at the pressure of  $1 \text{ atm}$ . At the top boundary, the air has a density of  $1.17 \text{ kg/m}^3$  at the atmospheric pressure of  $1 \text{ atm}$ . At  $5$  Celcius degrees, air and water have viscosity of  $18.45e^{-3} \text{ mPa s}$  and  $1 \text{ mPa s}$  respectively. On all boundary faces, the symmetric boundary condition is imposed, while the Neuman boundary condition is imposed at the top boundary for pressure ( $dp/dx = 0 \text{ kPa}$ ) and density ( $d/dx = 0 \text{ kg/m}^3$ ).



*Figure 15: Shear strain during the earthquake-induced submarine landslides*

We demonstrate the entire process and the mechanism of the earthquake-induced submarine landslides by showing the shear strain (Figure 15), the pore water pressure in atm (Figure 16) and the velocity (Figure 17). The failure mechanism can be characterized as the progressive failure mechanism. Here are some numerical observations:

1. At the initial of the seismic event, the seismic loading triggers the first slide at 3 seconds. At 10 seconds, the debris start to move with the maximum speed of around 2-3 m/s with multiple shear band developed in the slope. The wave generated from the submarine slide is around 2-3m towards the slide direction.

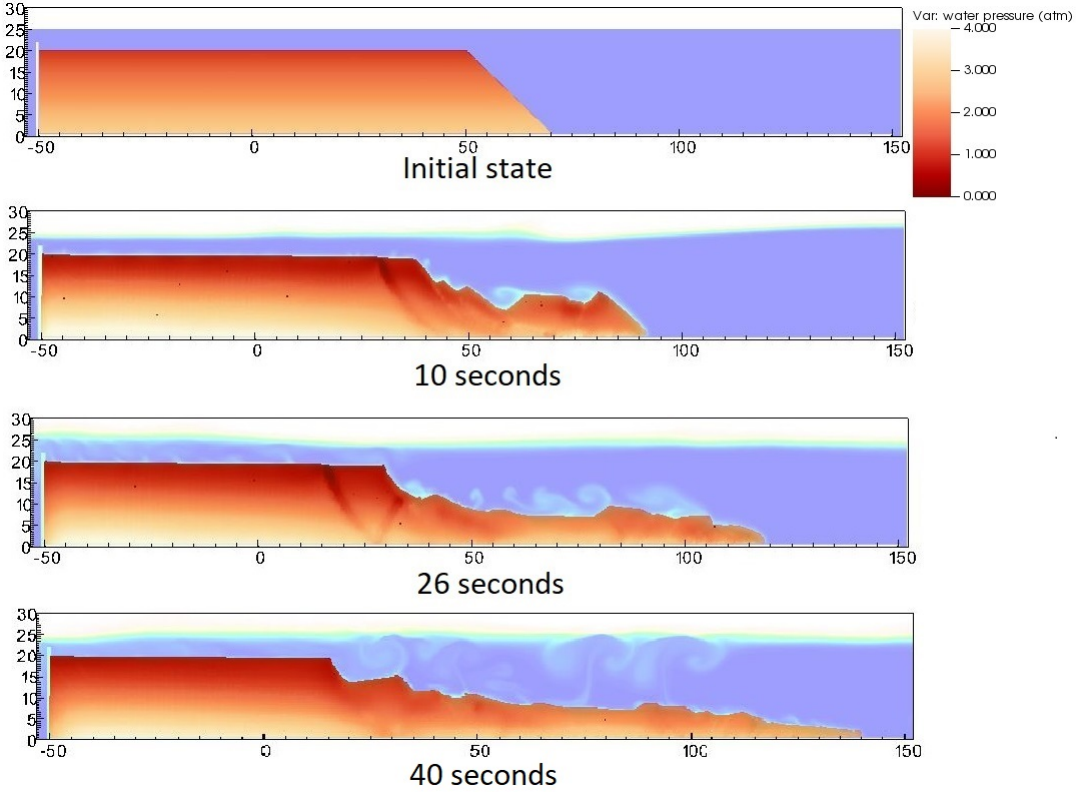
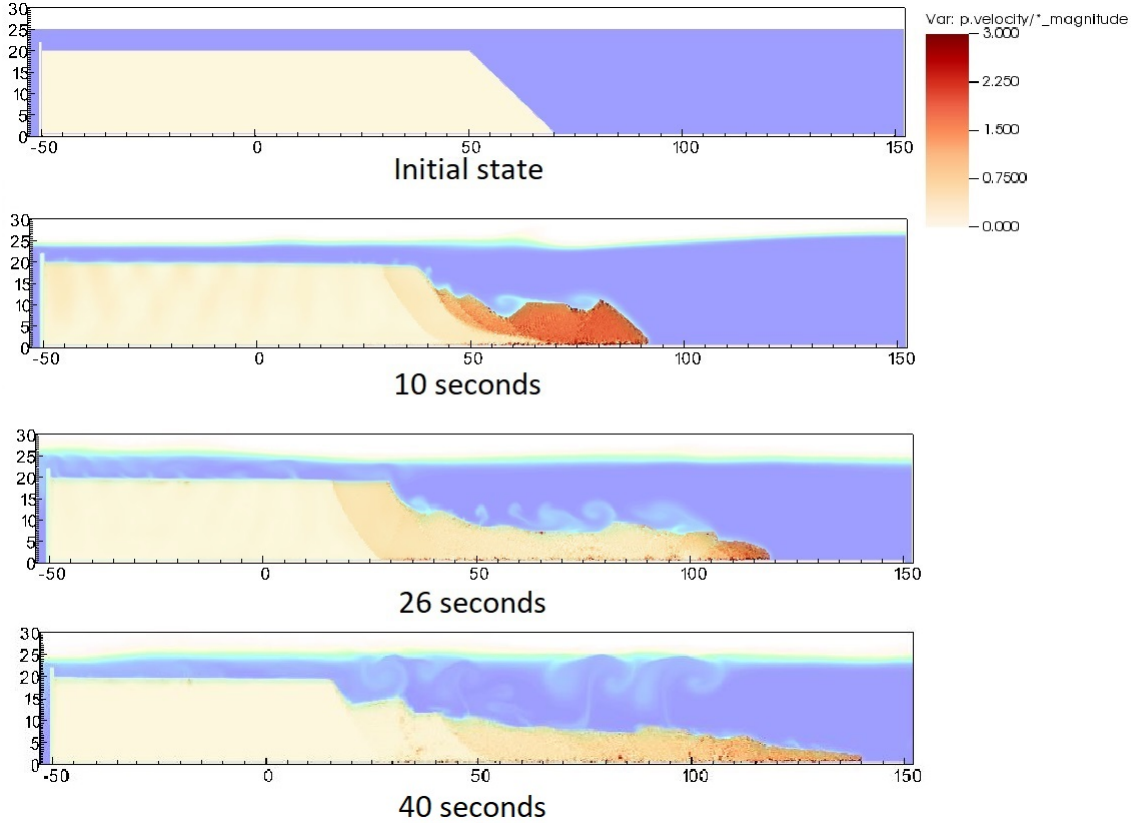


Figure 16: pore water pressure during the earthquake-induced submarine landslides

2. When the onset of the failure occurs in the slope (for example at 10 seconds and 26 seconds), the negative excess pore water pressure is developed along the shear band of the slope with pore water pressure is under 1atm. This is a typical dilatancy behavior when the soil is sheared rapidly in the undrained behavior.
3. When the seismic loading ends at 23 seconds, the last shear band is mobilized and the slope soon reaches to the final deposition. No more progressive failure developed in the slope. The turbulent flow developed as the interaction between debris flow and seawater.

Overall, we show the completed process of the earthquake-induced submarine landslides involving (1) earthquake triggering mechanism, (2) the onset of the shear band with the development of negative excess pore water pressure, (3) progressive failure mechanism, (4) submarine landslide induced wave to final deposition.



*Figure 17: Velocity during the earthquake-induced submarine landslides*

## Conclusions

We have presented a numerical approach MPMICE for the simulation of large deformation soil-fluid-structure interaction, emphasizing the simulation of the earthquake-induced submarine landslides. The model uses (1) the Material Point Method for capturing the large deformation of iso-thermal porous media and solid structures and (2) Implicit Continuous Eulerian (compressible, conservative multi-material CFD formulation) for modeling the complex fluid flow including turbulence. This model is implemented in the high-performance Uintah computational framework and validated against analytical solution and experiment. We then demonstrate the capability of the model to simulate the entire process of the earthquake induced submarine landslides.

## Acknowledgements

The authors gratefully acknowledge Dr. James Guilkey and Dr. Todd Harman from the University of Utah for sharing the insight on the theoretical framework of MPMICE which this work is based. This project has received funding from the European Union’s Horizon 2020 research and innovation program under the Marie Skłodowska-Curie Actions (MSCA) Individual Fellowship (Project SUBSLIDE “Submarine landslides and their impacts on offshore infrastructures”) grant agreement 101022007. The authors would also like to acknowledge the support from the Research Council of Norway through its Centers of Excellence funding scheme, project number 262644 Porelab. The computations were performed on High Performance Computing resources provided by UNINETT Sigma2 - the National Infrastructure for High Performance Computing and Data Storage in Norway.

## Appendix

Before deriving the governing equation, we give some definition (following [16]) as below:

$$-\frac{1}{V} \left[ \frac{\partial V}{\partial p} \right] \equiv \kappa_f \quad \text{isothermal compressibility of fluid} \quad (86)$$

$$\frac{1}{V} \left[ \frac{\partial V}{\partial T} \right] \equiv \alpha_f \quad \text{constant pressure thermal expansivity of fluid} \quad (87)$$

Then, the rate of volume with incompressible solid grains are calculated as below:

$$\begin{aligned} \frac{1}{V} \frac{D_f V}{Dt} &= \frac{1}{V} \left( \left[ \frac{\partial V}{\partial p} \right] \frac{D_f p}{Dt} + \left[ \frac{\partial V}{\partial T} \right] \frac{D_f T}{Dt} \right) = \frac{1}{V} \left( -\kappa \frac{D_f p}{Dt} + \alpha \frac{D_f T}{Dt} \right) \\ &= -(-\nabla \cdot \mathbf{U}_f + \alpha_f \frac{D_f T_f}{Dt}) + \alpha_f \frac{D_f T_f}{Dt} = \nabla \cdot \mathbf{U}_f \end{aligned} \quad (88)$$

$$\frac{1}{V} \frac{D_s V}{Dt} = \nabla \cdot \mathbf{U}_s \quad (89)$$

It is also convenient to define the Lagrangian derivative for a state variable  $f$  as:

$$\frac{D_f f}{Dt} = \frac{\partial f}{\partial t} + \mathbf{U}_f \cdot \nabla f \quad \frac{D_s f}{Dt} = \frac{\partial f}{\partial t} + \mathbf{U}_s \cdot \nabla f \quad (90)$$

### *Evolution of porosity*

Solving the solid mass balance equation (4) with the definition of solid mass in equation (2), it leads to the rate of porosity as below:

$$\frac{D_s m_s}{Dt} = \frac{D_s((1-n)\rho_s V)}{Dt} = \rho_s V \frac{D_s(1-n)}{Dt} + (1-n)V \frac{D_s \rho_s}{Dt} + (1-n)\rho_s \frac{D_s V}{Dt} = 0 \quad (91)$$

The soil grains are assumed to be incompressible, therefore, term 2 in the right hand side is zero.

$$V \frac{D_s(1-n)}{Dt} + (1-n) \frac{D_s V}{Dt} = 0 \quad (92)$$

Dividing all terms with  $V$  with the equation (88), it leads to:

$$\frac{D_s n}{Dt} = \frac{\partial n}{\partial t} + \mathbf{U}_s \cdot \nabla n = (1-n) \nabla \cdot \mathbf{U}_s \quad (93)$$

Finally, we get:

$$\frac{\partial n}{\partial t} = (1-n) \nabla \cdot \mathbf{U}_s - \mathbf{U}_s \cdot \nabla n \quad (94)$$

### *Evolution of specific volume*

The restriction for the equilibrium pressure can be derived from:

$$\begin{aligned} 0 &= \frac{\partial}{\partial t} \left( n - \sum_{f=1}^{N_f} v_f \rho_f \right) = \frac{\partial n}{\partial t} - \sum_{f=1}^{N_f} \left( \rho_f \frac{\partial v_f}{\partial t} + v_f \frac{\partial \rho_f}{\partial t} \right) \\ &= \frac{\partial n}{\partial t} - \sum_{f=1}^{N_f} \left( \rho_f \frac{D_f v_f}{Dt} + \nabla \cdot (v_f \rho_f \mathbf{U}_f) \right) \end{aligned} \quad (95)$$

Since the equation of state shows that:

$$\frac{D_f v_f}{Dt} = v_f \left( \kappa_f \frac{D_f P_{eq}}{Dt} + \alpha_f \frac{D_f T_f}{Dt} \right) \quad (96)$$

Then equation (95) becomes:

$$0 = \frac{\partial n}{\partial t} - \sum_{f=1}^{N_f} \left( \rho_f v_f \left( \kappa_f \frac{D_f P_{eq}}{Dt} + \alpha_f \frac{D_f T_f}{Dt} \right) + \nabla \cdot (v_f \rho_f \mathbf{U}_f) \right) \quad (97)$$

Putting equation (94) into equation (97) leads to:

$$\sum_{f=1}^{N_f} \phi_f \kappa_f \frac{D_f P_{eq}}{Dt} = -\nabla \cdot \mathbf{U} + \sum_{f=1}^{N_f} \phi_f \alpha_f \frac{D_f T_f}{Dt} \quad (98)$$

where  $\mathbf{U} = \nabla \cdot (\sum_{s=1}^{N_s} \phi_s \mathbf{U}_s + \sum_{f=1}^{N_f} \phi_f \mathbf{U}_f)$ . And the rate of the specific volumne is computed by putting equation (98) into equation (96):

$$\bar{\rho}_f \frac{D_f v_f}{Dt} = f_f^\phi \nabla \cdot \mathbf{U} + (\phi_f \alpha_f \frac{D_f T_f}{Dt} - f_f^\phi \sum_{n=1}^N \phi_n \alpha_n \frac{D_n T_n}{Dt}) \quad (99)$$

where  $f_f^\phi = (\phi_f \kappa_f) / (\sum_{n=1}^N \phi_n \kappa_n)$  with  $\kappa_f$  being f-material bulk compressibility.

#### *Momentum conservation*

The linear momentum balance equation for the fluid phase based on mixture theory is:

$$\frac{1}{V} \frac{D_f(m_f \mathbf{U}_f)}{Dt} = \nabla \cdot (-np_f \mathbf{I}) + \nabla \cdot \boldsymbol{\tau}_f + \bar{\rho}_f \mathbf{b} + \mathbf{f}_d + \mathbf{f}_b \quad (100)$$

On the right hand sand, the first term is the divergence of partial fluid phase stress, the second term is the body force, the third term is the drag force (momentum exchange) and the fourth term is the buoyant force described in [22] for the immiscible mixtures. The buoyant force is in the form:

$$\mathbf{f}_b = \boldsymbol{\sigma}_f \nabla(n) \quad (101)$$

As a result, the linear momentum balance equation for fluid phase becomes:

$$\frac{1}{V} \frac{D_f(m_f \mathbf{U}_f)}{Dt} = -n \nabla p_f + \nabla \cdot \boldsymbol{\tau}_f + \bar{\rho}_f \mathbf{b} + \mathbf{f}_d \quad (102)$$

The Reynolds stress component can be included in the term  $\boldsymbol{\tau}_f$  to consider the turbulent effects if needed. To derive the linear momentum balance equation for the solid phase, we begin with the linear momentum balance equation for the mixture as:

$$\frac{1}{V} \frac{D_f(m_f \mathbf{U}_f)}{Dt} + \frac{1}{V} \frac{D_s(m_s \mathbf{U}_s)}{Dt} = \nabla \cdot (\boldsymbol{\sigma}) + \bar{\rho}_f \mathbf{b} + \bar{\rho}_s \mathbf{b} \quad (103)$$

Combining Terzaghi's equation (3) and subtracting both sides with equation (102), we obtain the linear momentum balance equation for the solid phase as:

$$\nabla \cdot (\boldsymbol{\sigma}') - (1-n)\nabla p_f + \bar{\rho}_s \mathbf{b} - \mathbf{f}_d \quad (104)$$

### *Energy conservation*

We adopt the general form of the total energy balance equation for the porous media from [23], the total energy balance equation for the fluid phase is:

$$\frac{1}{V} \frac{D_f(m_f(e_f + 0.5\mathbf{U}_f^2))}{Dt} = \nabla \cdot (-np_f \mathbf{I}) \cdot \mathbf{U}_f + \nabla \cdot \mathbf{q}_f + (\bar{\rho}_f \mathbf{b}) \cdot \mathbf{U}_f + \mathbf{f}_d \cdot \mathbf{U}_f + q_{sf} \quad (105)$$

Applying the product rule  $D(m\mathbf{U}^2) = D(m\mathbf{U} \cdot \mathbf{U}) = 2\mathbf{U} \cdot D(m\mathbf{U})$ , the left hand side of equation (105) becomes:

$$\frac{1}{V} \frac{D_f(m_f(e_f + 0.5\mathbf{U}_f^2))}{Dt} = \frac{1}{V} \frac{D_f(m_f e_f)}{Dt} + \frac{1}{V} \frac{D_f(m_f \mathbf{U}_f)}{Dt} \cdot \mathbf{U}_f \quad (106)$$

Combining equations (102), (105), (106), we obtain the final form of the internal energy balance equation for the fluid phase as:

$$\frac{1}{V} \frac{D_f(m_f e_f)}{Dt} = -\bar{\rho}_f p \frac{D_f v_f}{Dt} + \nabla \cdot \mathbf{q}_f + q_{sf} \quad (107)$$

On the right hand side, the terms include the average pressure-volume work, the average viscous dissipation, the thermal transport and the energy exchange between solid and fluid respectively. The heat flux is  $\mathbf{q}_f = \bar{\rho}_f \alpha_f \nabla T_f$ . To derive the internal energy balance equation for the solid phase, we begin with the total energy balance equation for the mixture based on [23] as:

$$\begin{aligned} & \frac{1}{V} \frac{D_f(m_f(e_f + 0.5\mathbf{U}_f^2))}{Dt} + \frac{1}{V} \frac{D_s(m_s(e_s + 0.5\mathbf{U}_s^2))}{Dt} = \nabla \cdot (-np_f \mathbf{I}) \cdot \mathbf{U}_f \\ & + \nabla \cdot (\boldsymbol{\sigma}' - (1-n)p_f \mathbf{I}) \cdot \mathbf{U}_s + (-np_f \mathbf{I}) : \nabla \mathbf{U}_f + (\boldsymbol{\sigma}' - (1-n)p_f \mathbf{I}) : \nabla \mathbf{U}_s \\ & + (\bar{\rho}_f \mathbf{b}) \cdot \mathbf{U}_f + (\bar{\rho}_s \mathbf{b}) \cdot \mathbf{U}_s + \nabla \cdot \mathbf{q}_f + \nabla \cdot \mathbf{q}_s + \mathbf{f}_d \cdot (\mathbf{U}_f - \mathbf{U}_s) \end{aligned} \quad (108)$$

Subtracting equation (108) to equations (105) and (104), we obtained the internal energy balance equation for solid phase as:

$$\frac{1}{V} \frac{D_s(m_s e_s)}{Dt} = \boldsymbol{\sigma}' : \nabla \mathbf{U}_s + \nabla \cdot \mathbf{q}_s - q_{sf} \quad (109)$$

On the right hand side, he terms include the mechanical work, thermal transport and energy exchange between solid and fluid respectively. The heat flux is  $\mathbf{q}_s = \bar{\rho}_s \alpha_s \nabla T_s$

### *Advanced Fluid Pressure*

The discretization of the pressure equation begins with the Lagrangian face-centered velocity and the equation for the pressure

$$\bar{\rho}_{f,FC} \frac{\mathbf{U}_{f,FC}^{n+1} - \mathbf{U}_{f,FC}^n}{\Delta t} = n \nabla^{FC} P_{fc}^{n+1} + \bar{\rho}_{f,FC} \mathbf{b} \quad (110)$$

$$\kappa \frac{dP}{dt} = \nabla^c \cdot \mathbf{U}_{f,FC}^{n+1} \quad (111)$$

The divergence of the equation (110) with  $\nabla \cdot \mathbf{b} = 0$  is

$$\nabla^c \cdot \mathbf{U}_{f,FC}^{n+1} - \nabla^c \cdot \mathbf{U}_{f,FC}^n = \nabla^c \frac{\Delta t}{\rho_{f,FC}^n} \cdot \nabla^{FC} (P_{fc}^n + \Delta P_{fc}^n) \quad (112)$$

To solve this equation, we define the face-centered intermediate velocity  $\mathbf{U}_{f,FC}^*$  as:

$$\bar{\rho}_{f,FC} \frac{\mathbf{U}_{f,FC}^* - \mathbf{U}_{f,FC}^n}{\Delta t} = n \nabla^{FC} P_{fc}^n + \bar{\rho}_{f,FC} \mathbf{b} \quad (113)$$

The divergence of the equation (113) is

$$\nabla^c \cdot \mathbf{U}_{f,FC}^* - \nabla^c \cdot \mathbf{U}_{f,FC}^n = \nabla^c \frac{\Delta t}{\rho_{f,FC}^n} \cdot \nabla^{FC} P_{fc}^n \quad (114)$$

Combining equations (111, 112, 114), it leads to

$$\left( \kappa - \nabla^c \frac{\Delta t}{\rho_{f,FC}^n} \cdot \nabla^{FC} \right) \Delta P_{fc}^n = -\nabla^c \cdot \mathbf{U}_{f,FC}^* \quad (115)$$

When the fluid is incompressible,  $\kappa$  approaches to zero and the equation (115) becomes the Poisson's equation for the incompressible fluid flow.

### Momentum exchange with an implicit solve

Considering the fluid momentum balance equation as

$$(m\mathbf{U})_{f,FC}^{n+1} = (m\mathbf{U})_{f,FC}^n - \Delta t(Vn\nabla^{FC}P_{fc}^n + m_f\mathbf{b}) + VK\Delta t(\mathbf{U}_{s,FC}^{n+1} - \mathbf{U}_{f,FC}^{n+1}) \quad (116)$$

Assuming  $m_{f,FC}^{n+1} = m_{f,FC}^n$  we get

$$\mathbf{U}_{f,FC}^{n+1} = \mathbf{U}_{f,FC}^n - \Delta t\left(\frac{\nabla^{FC}P_{fc}^n}{\rho_{f,FC}^n} + \mathbf{b}\right) + \frac{\Delta tK}{\bar{\rho}_{f,FC}^n}(\mathbf{U}_{s,FC}^{n+1} - \mathbf{U}_{f,FC}^{n+1}) \quad (117)$$

As defined in the section 'Advanced Fluid Pressure', the face-centered intermediate fluid velocity  $\mathbf{U}_{f,FC}^* = \Delta t(\nabla^{FC}P_{fc}^n/\rho_{f,FC}^n + \mathbf{b})$  leading to

$$\mathbf{U}_{f,FC}^{n+1} = \mathbf{U}_{f,FC}^* + \frac{\Delta tK}{\bar{\rho}_{f,FC}^n}(\mathbf{U}_{s,FC}^{n+1} - \mathbf{U}_{f,FC}^{n+1}) \quad (118)$$

Considering the solid momentum balance equation as

$$(m\mathbf{U})_{s,FC}^{n+1} = (m\mathbf{U})_{s,FC}^n - \Delta t(V\nabla^{FC}\cdot\boldsymbol{\sigma}'^n - V(1-n)\nabla^{FC}P_{fc}^n + m_s\mathbf{b}) - VK\Delta t(\mathbf{U}_{s,FC}^{n+1} - \mathbf{U}_{f,FC}^{n+1}) \quad (119)$$

We define the face-centered intermediate solid velocity as  $\mathbf{U}_{s,FC}^* = \Delta t(\nabla^{FC}\cdot\boldsymbol{\sigma}'^n/\bar{\rho}_{s,FC} - \nabla^{FC}P_{fc}^n/\rho_s + \mathbf{b})$  leading to

$$\mathbf{U}_{s,FC}^{n+1} = \mathbf{U}_{s,FC}^* - \frac{\Delta tK}{\bar{\rho}_{s,FC}^n}(\mathbf{U}_{s,FC}^{n+1} - \mathbf{U}_{f,FC}^{n+1}) \quad (120)$$

Combining equation (118) and (120) we get

$$\begin{aligned} \mathbf{U}_{f,FC}^* + \Delta\mathbf{U}_{f,FC} &= \mathbf{U}_{f,FC}^* + \frac{\Delta tK}{\bar{\rho}_{f,FC}^n}(\mathbf{U}_{s,FC}^* + \Delta\mathbf{U}_{s,FC} - \mathbf{U}_{f,FC}^* - \Delta\mathbf{U}_{f,FC}) \\ \mathbf{U}_{s,FC}^* + \Delta\mathbf{U}_{s,FC} &= \mathbf{U}_{s,FC}^* - \frac{\Delta tK}{\bar{\rho}_{s,FC}^n}(\mathbf{U}_{s,FC}^* + \Delta\mathbf{U}_{s,FC} - \mathbf{U}_{f,FC}^* - \Delta\mathbf{U}_{f,FC}) \end{aligned} \quad (121)$$

Rearranging the equation (121), it leads to the linear system of equations

$$\begin{vmatrix} (1 + \beta_{12,FC}) & -\beta_{12,FC} \\ -\beta_{21,FC} & (1 + \beta_{21,FC}) \end{vmatrix} \begin{vmatrix} \Delta\mathbf{U}_{f,FC} \\ \Delta\mathbf{U}_{s,FC} \end{vmatrix} = \begin{vmatrix} \beta_{12,FC}(\mathbf{U}_{s,FC}^* - \mathbf{U}_{f,FC}^*) \\ \beta_{21,FC}(\mathbf{U}_{f,FC}^* - \mathbf{U}_{s,FC}^*) \end{vmatrix}$$

Solving this linear equations with  $\beta_{12,FC} = (\Delta t K) / \bar{\rho}_{f,FC}^n$  and  $\beta_{21,FC} = (\Delta t K) / \bar{\rho}_{s,FC}^n$ . Similar derivation can be performed to computed the cell-center velocity increment leading to

$$\begin{vmatrix} (1 + \beta_{12c}) & -\beta_{12c} \\ -\beta_{21c} & (1 + \beta_{21c}) \end{vmatrix} \begin{vmatrix} \Delta \mathbf{U}_{fc} \\ \Delta \mathbf{U}_{sc} \end{vmatrix} = \begin{vmatrix} \beta_{12c}(\mathbf{U}_{sc}^* - \mathbf{U}_{fc}^*) \\ \beta_{21c}(\mathbf{U}_{fc}^* - \mathbf{U}_{sc}^*) \end{vmatrix}$$

with  $\beta_{12c} = (\Delta t K) / \bar{\rho}_{fc}^n$  and  $\beta_{21c} = (\Delta t K) / \bar{\rho}_{sc}^n$  and the cell-centered intermediate velocity can be calculated by

$$\begin{aligned} \mathbf{U}_{fc}^* &= \mathbf{U}_{fc}^n + \Delta t \left( -\frac{\nabla P_{fc}^{n+1}}{\rho_{fc}^n} + \frac{\nabla \cdot \boldsymbol{\tau}_{fc}^n}{\bar{\rho}_{fc}^n} + \mathbf{b} \right) \\ \mathbf{U}_{sc}^* &= \mathbf{U}_{sc}^n + \Delta t \left( \frac{\nabla \cdot \boldsymbol{\sigma}_c'^n}{\bar{\rho}_{sc}^n} - \frac{\nabla P_{sc}^{n+1}}{\rho_s} + \mathbf{b} \right) \end{aligned} \quad (122)$$

## References

- [1] D. Yuk, S. Yim, P.-F. Liu, Numerical modeling of submarine mass-movement generated waves using RANS model, *Computers and Geosciences* 32 (7) (2006) 927–935. doi:10.1016/j.cageo.2005.10.028.  
URL <https://doi.org/10.1016/j.cageo.2005.10.028>
- [2] S. Glimsdal, J.-S. L’Heureux, C. B. Harbitz, F. Løvholt, The 29th january 2014 submarine landslide at statland, norway—landslide dynamics, tsunami generation, and run-up, *Landslides* 13 (6) (2016) 1435–1444. doi:10.1007/s10346-016-0758-7.  
URL <https://doi.org/10.1007/s10346-016-0758-7>
- [3] S. Abadie, D. Morichon, S. Grilli, S. Glockner, Numerical simulation of waves generated by landslides using a multiple-fluid navier–stokes model, *Coastal Engineering* 57 (9) (2010) 779–794. doi:10.1016/j.coastaleng.2010.03.003.  
URL <https://doi.org/10.1016/j.coastaleng.2010.03.003>
- [4] M. Rauter, S. Viroulet, S. S. Gylfadóttir, W. Fellin, F. Løvholt, Granular porous landslide tsunami modelling – the 2014 lake askja flank collapse, *Nature Communications* 13 (1) (Feb. 2022). doi:10.1038/s41467-022-28296-7.  
URL <https://doi.org/10.1038/s41467-022-28296-7>

- [5] Q.-A. Tran, W. Sołowski, Generalized interpolation material point method modelling of large deformation problems including strain-rate effects – application to penetration and progressive failure problems, *Computers and Geotechnics* 106 (2019) 249–265. doi:10.1016/j.compgeo.2018.10.020.  
 URL <https://doi.org/10.1016/j.compgeo.2018.10.020>
- [6] T. Capone, A. Panizzo, J. J. Monaghan, SPH modelling of water waves generated by submarine landslides, *Journal of Hydraulic Research* 48 (sup1) (2010) 80–84. doi:10.1080/00221686.2010.9641248.  
 URL <https://doi.org/10.1080/00221686.2010.9641248>
- [7] X. Zhang, E. Oñate, S. A. G. Torres, J. Bleyer, K. Krabbenhoft, A unified lagrangian formulation for solid and fluid dynamics and its possibility for modelling submarine landslides and their consequences, *Computer Methods in Applied Mechanics and Engineering* 343 (2019) 314–338. doi:10.1016/j.cma.2018.07.043.  
 URL <https://doi.org/10.1016/j.cma.2018.07.043>
- [8] R. Dey, B. C. Hawlader, R. Phillips, K. Soga, Numerical modelling of submarine landslides with sensitive clay layers, *Géotechnique* 66 (6) (2016) 454–468. doi:10.1680/jgeot.15.p.111.  
 URL <https://doi.org/10.1680/jgeot.15.p.111>
- [9] S. Bandara, K. Soga, Coupling of soil deformation and pore fluid flow using material point method, *Computers and Geotechnics* 63 (2015) 199–214. doi:10.1016/j.compgeo.2014.09.009.  
 URL <https://doi.org/10.1016/j.compgeo.2014.09.009>
- [10] A. P. Tampubolon, T. Gast, G. Klár, C. Fu, J. Teran, C. Jiang, K. Museth, Multi-species simulation of porous sand and water mixtures, *ACM Transactions on Graphics* 36 (4) (2017) 1–11. doi:10.1145/3072959.3073651.  
 URL <https://doi.org/10.1145/3072959.3073651>
- [11] A. S. Baumgarten, K. Kamrin, A general constitutive model for dense, fine-particle suspensions validated in many geometries, *Proceedings of the National Academy of Sciences* 116 (42) (2019) 20828–20836. doi:10.1073/pnas.1908065116.  
 URL <https://doi.org/10.1073/pnas.1908065116>

- [12] Q.-A. Tran, W. Sołowski, Temporal and null-space filter for the material point method, *International Journal for Numerical Methods in Engineering* 120 (3) (2019) 328–360. doi:10.1002/nme.6138.  
 URL <https://doi.org/10.1002/nme.6138>
- [13] X. Zheng, F. Pisanò, P. J. Vardon, M. A. Hicks, An explicit stabilised material point method for coupled hydromechanical problems in two-phase porous media, *Computers and Geotechnics* 135 (2021) 104112. doi:10.1016/j.compgeo.2021.104112.  
 URL <https://doi.org/10.1016/j.compgeo.2021.104112>
- [14] Q. A. Tran, W. Sołowski, M. Berzins, J. Guilkey, A convected particle least square interpolation material point method, *International Journal for Numerical Methods in Engineering* 121 (6) (2019) 1068–1100. doi:10.1002/nme.6257.  
 URL <https://doi.org/10.1002/nme.6257>
- [15] J.-S. Chen, M. Hillman, S.-W. Chi, Meshfree methods: Progress made after 20 years, *Journal of Engineering Mechanics* 143 (4) (Apr. 2017). doi:10.1061/(asce)em.1943-7889.0001176.  
 URL [https://doi.org/10.1061/\(asce\)em.1943-7889.0001176](https://doi.org/10.1061/(asce)em.1943-7889.0001176)
- [16] B. A. Kashiwa, A multifield model and method for fluid-structure interaction dynamics, Tech. Rep. LA-UR-01-1136, Los Alamos National Laboratory (2001).
- [17] J. Guilkey, T. Harman, B. Banerjee, An eulerian-lagrangian approach for simulating explosions of energetic devices, *Computers and Structures* 85 (11) (2007) 660 – 674. doi:<https://doi.org/10.1016/j.compstruc.2007.01.031>.  
 URL <http://www.sciencedirect.com/science/article/pii/S0045794907000429>
- [18] A. S. Baumgarten, B. L. Couchman, K. Kamrin, A coupled finite volume and material point method for two-phase simulation of liquid–sediment and gas–sediment flows, *Computer Methods in Applied Mechanics and Engineering* 384 (2021) 113940. doi:10.1016/j.cma.2021.113940.  
 URL <https://doi.org/10.1016/j.cma.2021.113940>
- [19] J. A. M. K. R. Beetstra, M. A. van der Hoef, Drag force of intermediate reynolds number flow past mono- and bidisperse arrays of spheres,

Fluid Mechanics and Transport Phenomena 53 (2) (2007) 489 – 501.  
doi:<https://doi.org/10.1002/aic.11065>.

- [20] S. Bardenhage, J. Guilkey, K. Roessig, J. Brackbill, W. Witzel, J.C.Foster, An improved contact algorithm for the material point method and application to stress propagation in granular material, CMES-Computer Modeling in Engineering and Sciences 2 (2001) 509–522. doi:[10.3970/cmes.2001.002.509](https://doi.org/10.3970/cmes.2001.002.509).
- [21] S. A. R. C. Mariotti;, P. Heinrich, Numerical simulation of submarine landslides and their hydraulic effects, Journal of Waterway, Port, Coastal, and Ocean Engineering 123 (4) (1997). doi:[https://doi.org/10.1061/\(ASCE\)0733-950X\(1997\)123:4\(149\)](https://doi.org/10.1061/(ASCE)0733-950X(1997)123:4(149)).
- [22] D. Drumheller, On theories for reacting immiscible mixtures, International Journal of Engineering Science 38 (3) (2000) 347 – 382. doi:[https://doi.org/10.1016/S0020-7225\(99\)00047-6](https://doi.org/10.1016/S0020-7225(99)00047-6).  
URL <http://www.sciencedirect.com/science/article/pii/S0020722599000476>
- [23] S. Hassanzadeh, Derivation of basic equations of mass transport in porous media, part1: Macroscopic balance laws, Advances in Water Resources 9 (1986) 196–206. doi:[https://doi.org/10.1016/0309-1708\(86\)90024-2](https://doi.org/10.1016/0309-1708(86)90024-2).